Powerful combination of g-C_3N_4 and LDHs for enhanced photocatalytic performance: a review of strategy, synthesis, and applications

Biao Song[a,1], Zhuotong Zeng[b,1], Guangming Zeng[a,*], Jilai Gong[a,*], Rong Xiao[b,*], Shujing Ye[a], Ming Chen[a], Cui Lai[a], Piao Xu[a], Xiang Tang[a]

[a] College of Environmental Science and Engineering, Hunan University, and Key Laboratory of Environmental Biology and Pollution Control (Hunan University), Ministry of Education, Changsha 410082, PR China

[b] Department of Dermatology, Second Xiangya Hospital, Central South University, Changsha 410011, PR China

* Corresponding authors.

E-mail addresses: zgming@hnu.edu.cn (G. Zeng), jilaigong@hnu.edu.cn (J. Gong), and xiaorong65@csu.edu.cn (R. Xiao)

[1] These authors contribute equally to this article.

Abstract

The utilization of solar energy with photocatalytic technology has been considered a good solution to alleviate environmental pollution and energy shortage. Constructing 2D/2D heterostructure photocatalysts with layered double hydroxide (LDH) and graphitic carbon nitride (g-C_3N_4) is an effective approach to attain high performance in solar photocatalysis. This paper provides a review of recent studies about 2D/2D LDH/g-C_3N_4 heterostructure photocatalysts. Main strategies for constructing the desired 2D/2D heterojunction are summarized. The planar structure of LDH and g-C_3N_4 offers a shorter transfer distance for charge carriers and reduces electron-hole recombination in the bulk phase. The face-to-face contact between the two materials can promote the charge transfer across the heterostructure interface, thus improving the electron-hole separation efficiency. The performance and mechanisms of LDH/g-C_3N_4 photocatalysts in hydrogen production, CO_2 reduction, and organic pollutant degradation are analyzed and discussed. Incorporating reduced graphene oxide or Ag nanoparticles into LDH/g-C_3N_4 heterojunction and fabricating calcined LDH/g-C_3N_4 composites are effective strategies to further facilitate charge transfer at the interface of LDH and g-C_3N_4 and improve the absorption capacity for visible light. This review is expected to provide basic insights into the design of 2D/2D LDH/g-C_3N_4 heterojunctions and their applications in solar photocatalysis.

Keywords: Carbon nitride; Layered double hydroxide; 2D/2D heterojunction; Photocatalysis; Visible light

1. Introduction

Environmental pollution and energy shortage have brought great challenges to human sustainable development [1-6]. Exploiting clean and renewable solar energy with photocatalytic technology has been widely considered one of promising solutions to the problems [7-12]. Photocatalytic technology can utilize solar irradiation to realize organic pollutant degradation [13, 14], Cr(VI) reduction [15, 16], and bacterial inactivation [17, 18], which provides a great way for pollution abatement. Additionally, considerable effort is being directed at photocatalytic hydrogen production and CO_2 reduction for converting solar energy to chemical energy [19-22]. If this technology can be applied in large scale, the energy crisis will be effectively alleviated. Photocatalytic reaction is essentially a photoinduced redox process. Photocatalyst is the core of photocatalytic technology, and plays a vital role in harvesting light and driving the reaction [23-26]. Thus, the study of high-efficient photocatalyst is essential for the development of photocatalytic technology.

Graphitic carbon nitride (g-C_3N_4) is a polymer semiconductor with triazine or heptazine as a basic structural unit, and has a graphite-like layer structure [27, 28]. Since its application in photocatalytic hydrogen production was first reported [29], g-C_3N_4 has attracted wide attention and been extensively researched for photocatalytic applications [30-33]. Compared with conventional photocatalysts (e.g., TiO_2), the band gap of g-C_3N_4 is smaller (~2.7 eV), which allows it to function under visible light [33]. Additionally, the great chemical stability, high thermostability, cheap raw materials, and simple synthesis process make g-C_3N_4 competitive among various

photocatalytic materials [30]. Nevertheless, g-C_3N_4 faces many problems in its practical applications. Only blue and violet light (wavelength < 460 nm) can be absorbed by g-C_3N_4, which causes low utilization rate of solar energy [34]. Fast recombination of photoinduced electron-hole pairs in g-C_3N_4 decreases the redox ability [35]. The bulk structure of g-C_3N_4 leads to relatively small specific surface area [36]. These shortcomings limit the further development of g-C_3N_4 for photocatalytic applications. Many strategies have been used to improve the photocatalytic activity of g-C_3N_4, such as loading co-catalyst, doping element (e.g., Fe, Zn, P, and S), designing nanostructure, and constructing heterojunction [37-40]. Among these strategies, constructing heterostructure with other semiconductor materials is typically applied to facilitate the separation of charge carriers in g-C_3N_4. Due to the difference in Fermi level of two different semiconductors, charge carriers can move between the semiconductors when they contact with each other, which finally forms an internal electric field at the interface. The photoinduced electrons and holes can move directionally in the electric field, thus being separated effectively [41].

Recently, using layered double hydroxides (LDHs) to construct heterojunction with g-C_3N_4 has been found a highly effective strategy for enhancing the photocatalytic performance. LDHs are a class of two-dimensional (2D) materials of hydrotalcite-like clays, which are composed of positively charged host layers and exchangeable interlayer anions. They can be expressed by a general chemical formula $[M^{2+}_{1-x}M^{3+}_{x}(OH)_2](A^{n-})_{x/n}\cdot mH_2O$, where M^{2+} is divalent cation (e.g., Ca^{2+}, Co^{2+}, Fe^{2+},

Mg^{2+}, Ni^{2+}, and Zn^{2+}), M^{3+} is trivalent cation (e.g., Al^{3+}, Co^{3+}, Cr^{3+}, Fe^{3+}, Mn^{3+}, and Ni^{3+}), A^{n-} is interlayer anion (e.g., CO_3^{2-}, SO_4^{2-}, NO_3^-, and Cl^-), x is the molar ratio of trivalent cation in total cations [M^{3+} / (M^{2+} + M^{3+})], and m is the crystal water number for each LDH molecule [42, 43]. Due to the low cost, high chemical stability, adjustable composition and uniform distribution of metal cations, as well as exchangeable interlayer anions, LDHs and their calcined products have found applications in many fields including photocatalysis [44]. However, pure LDHs are dissatisfactory in photocatalytic processes due to the fast recombination of photoinduced electron-hole pairs [43]. Constructing LDH/g-C_3N_4 heterojunctions with clever design can overcome the disadvantages of g-C_3N_4 and LDHs, and obtain ideal photocatalysts with excellent performance. In this article, recent advances in 2D/2D LDH/g-C_3N_4 heterostructure photocatalysts and their applications for solar energy conversion and pollution abatement are carefully reviewed. The characteristics of 2D/2D LDH/g-C_3N_4 as photocatalysts are first summarized to provide better understanding of the strategy for constructing LDH/g-C_3N_4 heterostructures. Then, various methods to achieve effective assembly of LDH and g-C_3N_4 are introduced and discussed. The applications of LDH/g-C_3N_4 photocatalytic systems in H_2 production, CO_2 reduction, and organic pollutant degradation are reviewed and analyzed. Lastly, some future research needs in 2D/2D LDH/g-C_3N_4 heterostructure photocatalysts are proposed. This work may benefit the design of high-efficient LDH/g-C_3N_4 photocatalysts and their applications.

2. Characteristics of 2D/2D LDH/g-C_3N_4 as photocatalysts

Constructing 2D/2D heterostructure has been considered an effective way to enhance the photoctalytic activity of LDH/g-C_3N_4 composites. The 2D structure of LDHs and g-C_3N_4 offers plentiful surface active sites for constructing photocatalytic composites and substantially shortens the transfer distance of photoinduced charge carriers within the materials, which is advantageous to the photocatalytic reactions [45-48]. The tunable composition and band structure make LDHs excellent semiconductors for constructing photocatalytic heterojunctions with g-C_3N_4. By adjusting and controlling the M^{2+} and M^{3+} in LDHs, the band gap of LDHs can be in the range of 2.0–3.4 eV, which benefits the harvesting of visible light [49]. Abundant basic sites on LDHs enable the materials to be used as heterogeneous solid base catalysts for many chemical reactions, and the position of catalytic active sites and product selectivity are also tunable as the metal cations and interlayer anions can be artificially controlled [50, 51]. Additionally, it is relatively easy to design the number of layers and interlayer space of LDHs, and functionalize LDHs with g-C_3N_4 [47, 52]. Constructing 2D/2D heterostructure with LDHs and g-C_3N_4 can make good use of the photocatalytic characteristics of these two 2D materials. Compared with other types of photocatalysts, 2D/2D LDH/g-C_3N_4 heterostructure has many advantages (Fig. 1). (1) Because of face-to-face contact between the two semiconductors, photoinduced charge carriers can transfer more efficiently across the heterojunction interface, which is conducive to electron-hole separation in a single material [53, 54]. (2) The 2D LDHs and g-C_3N_4 have a higher surface area that can increase the contact between

photocatalyst and reaction substrate, as well as the light harvesting ability of the photocatalyst [55, 56]. (3) 2D/2D heterostructure takes advantage of short transfer distance of charge carriers within LDHs and g-C_3N_4, and decreases the electron-hole recombination in the bulk phase [57, 58]. (4) The band structure of 2D/2D LDH/g-C_3N_4 heterostructure is tunable, which makes the photocatalyst suitable for various application systems [59-61]. These merits greatly improve the photocatalytic performance and applications of 2D/2D LDH/g-C_3N_4 heterojunctions.

3. Construction of 2D/2D LDH/g-C_3N_4 heterojunctions

The design and synthesis of photocatalyst are of great importance to achieve a good photocatalytic performance. Based on the assembly strategies of LDHs and g-C_3N_4 and the desired 2D/2D structure, the constructing methods mainly include electrostatic self-assembly, in-situ coprecipitation, hydrothermal method, solvothermal method, and calcination method. The following sections provide detailed information about these synthesis methods.

3.1. Electrostatic self-assembly

Electrostatic self-assembly is commonly used for constructing layered composites. It makes use of the electrostatic interaction between differently charged materials [62]. In the self-assembly process, the electrostatic attraction between opposite charges mainly drives the assembly, and meanwhile the assembly of each layer is controlled due to the electrostatic repulsion between like charges. This method

has been successfully applied in synthesizing many 2D/2D photocatalysts [62-65]. The water suspension of pristine g-C_3N_4 is negatively charged because of the amine-group deprotonation [66], while the host layer of LDHs is positively charged because of the ordered arrangement of metal cations [67]. These properties provide the basis for constructing LDH/g-C_3N_4 heterojunctions via electrostatic self-assembly. In the synthesis process, LDH and g-C_3N_4 are generally synthesized and exfoliated to sheets separately before the self-assembly. Many methods for exfoliating LDHs through ultrasonic treatment or mechanical stirring have been reported, such as directly exfoliating LDHs in organic solvents (e.g., formamide) and exfoliating LDHs after they are intercalated with organic anions (e.g., dodecyl benzene sulfonate) [68]. Additionally, LDHs can also be exfoliated through hydrothermal method, and the key to effectively delaminate LDHs is that the LDHs must be newly prepared wet sample [69]. In the laboratory, photocatalytic g-C_3N_4 nanosheets are mainly obtained through sonication exfoliation of bulk g-C_3N_4 [70, 71].

Hong et al. [72] synthesized Mg-Al-LDH/g-C_3N_4 photocatalyst by electrostatic self-assembly (Fig. 2). In that study, the authors first synthesized g-C_3N_4 from urea by thermal polymerization and Mg-Al-LDH by precipitation with NaOH. Then, the g-C_3N_4 nanosheets and Mg-Al-LDH nanosheets were obtained through sonication exfoliation and hydrothermal method. According to the measurement, the obtained g-C_3N_4 suspension and Mg-Al-LDH suspension had a zeta potential of −27.3 mV and +52.7 mV, respectively. By directly mixing the two suspensions, the g-C_3N_4 nanosheets and Mg-Al-LDH nanosheets assembled via electrostatic interaction and

Mg-Al-LDH/g-C_3N_4 photocatalyst was obtained. For confirming the 2D/2D assembly of Mg-Al-LDH and g-C_3N_4, the authors observed the photocatalyst morphology by transmission electron microscope (TEM), and found that Mg-Al-LDH flakes were well distributed on g-C_3N_4 sheets. Nayak et al. [73] reported a weight impregnation method for synthesizing Ni-Fe-LDH/g-C_3N_4 composite. It is actually a self-assembly process via electrostatic interaction, but the process was somewhere different from the above one. In their experiments, Ni-Fe-LDH and g-C_3N_4 were first produced by coprecipitation method and thermal polymerization, respectively. When synthesizing the Ni-Fe-LDH, the NaOH solution was dropwise added and the resulting precipitate was vigorously stirred for 24 h, in order to obtain Ni-Fe-LDH easy to be exfoliated in the following procedure. Then, the obtained Ni-Fe-LDH and g-C_3N_4 were severally suspended in methanol and ultrasonically treated for 30 min to obtain nanosheet suspensions. The two suspensions were subsequently mixed and put in a fume cupboard to completely volatilize methanol and obtain the final product. Though electrostatic self-assembly offers a simple operation for constructing LDH/g-C_3N_4 photocatalyst, the assembly process is difficult to control and it is affected by many factors, such as material surface roughness and effective charges. Therefore, using this method alone for LDH/g-C_3N_4 synthesis was relatively few. However, the electrostatic interaction between LDHs and g-C_3N_4 was also involved in constructing LDH/g-C_3N_4 photocatalyst with many other methods.

195 *3.2. In-situ coprecipitation*

196 Coprecipitation is the simultaneous precipitation of two or more cations in a
197 homogeneous solution by adding a precipitating agent. This method has been an
198 important way to synthesize composites that contain two or more metals, due to the
199 simple operation, low cost, manageable reaction conditions, short synthesis time, and
200 good products with uniform composition [74-76]. Coprecipitation is also a commonly
201 used method for synthesizing LDHs [77]. The desired LDHs can be obtained by
202 adding alkaline liquor into the mixed solution of metal cations that are needed for the
203 host layer and subsequent aging of the resulting suspension. The mixed cation
204 solution or the alkaline liquor contains interlayer anions of the LDHs. The LDH size
205 can be tuned through changing the reaction conditions such as solution pH value,
206 temperature, and aging time. For constructing LDH/g-C_3N_4 by coprecipitation, the
207 basic strategy is to precipitate the metal cations in situ after they are adsorbed on the
208 g-C_3N_4 sheet via electrostatic attraction.

209 Liu et al. [56] successfully synthesized 2D/2D Zn-Cr-LDH/g-C_3N_4
210 heterojunction by in-situ coprecipitation. Fig. 3 illustrates the specific synthesis
211 process. The authors first synthesized modified g-C_3N_4 sheets from urea in the
212 presence of citric acid (denoted as g-C_3N_4-C(N) by the authors) and made them to a
213 suspension. Then, Zn^{2+} and Cr^{3+} were added to the suspension with stirring. In this
214 process, Zn^{2+} and Cr^{3+} were adsorbed on the g-C_3N_4-C(N) sheet through electrostatic
215 attraction. NaOH was subsequently added to precipitate Zn^{2+} and Cr^{3+} and form
216 Zn-Cr-LDH in situ on g-C_3N_4 surface. The authors further applied the

Zn-Cr-LDH/g-C_3N_4-C(N) product for photocatalytic degradation of Congo red, and the photocatalytic activity was higher than that with Zn-Cr-LDH or g-C_3N_4 as the photocatalyst. Arif et al. [78] synthesized Co-Mn-LDH/g-C_3N_4 heterojunction by a similar in-situ coprecipitation process. In the experimental section of their report, it was emphasized that the mixture of metal cations and g-C_3N_4 needed to be ultrasonically treated for over one hour to enable sufficient adsorption of Co^{2+} and Mn^{2+} on g-C_3N_4 sheets through electrostatic interaction. This treatment process is vital to ensure an effective in-situ coprecipitation. Yuan and Li [79] reported an in-situ crystallization method for fabricating Zn-Al-LDH/g-C_3N_4 composites. It is actually an in-situ coprecipitation process. In that study, Zn-Al-LDH crystals formed in situ on g-C_3N_4 sheets as the coprecipitation of Zn^{2+} and Al^{3+}. The authors observed the microstructure of Zn-Al-LDH/g-C_3N_4 by TEM and found that relatively large g-C_3N_4 sheet was uniformly covered with Zn-Al-LDH flakes. It was considered that g-C_3N_4 could act as a substrate to induce the LDH crystallite growth. Polar functional groups on g-C_3N_4 had a good affinity for metal cations, which was conducive to the enrichment of Zn^{2+} and Al^{3+} and the growth of Zn-Al-LDH crystals on the g-C_3N_4 sheets. According to these studies, electrostatic interaction and g-C_3N_4-induced crystallization are the main mechanisms of LDH/g-C_3N_4 synthesis by in-situ coprecipitation.

3.3. Hydrothermal method

Hydrothermal method, also termed hydrothermal synthesis, is a common technique for producing composite materials via chemical reactions that occur in aqueous solution in a pressure-tight reactor with high temperature and high pressure [80]. The main advantage of this method is that well-crystallized product can be easily obtained by a simple hydrothermal process [81]. Additionally, it is convenient to design the product morphology and structure through controlling the reaction conditions [82]. According to the reaction type, hydrothermal method can be further divided into hydrothermal oxidation, hydrothermal reduction, hydrothermal precipitation, hydrothermal decomposition, hydrothermal polymerization, and so on. For constructing LDH/g-C_3N_4 heterostructure, hydrothermal precipitation method was used in many studies. Some metal cations are difficult to form layered hydroxides by coprecipitation under mild temperature and pressure conditions, but the reaction is easier to occur in a hydrothermal system with high temperature and pressure. Furthermore, the resulting LDH/g-C_3N_4 products usually have a good 2D/2D morphology.

Liu et al. [83] synthesized Zn-Cr-LDH/g-C_3N_4 composite by a hydrothermal method (Fig. 4). In their experiments, g-C_3N_4 nanosheet suspension was obtained through ultrasonic treatment of bulk g-C_3N_4, which was prepared through thermal polymerization with urea as the raw material. Then, Zn^{2+}, Cr^{3+}, and alkaline liquor (NaOH and Na_2CO_3) were added to the suspension. The hydrothermal reaction was carried out in a Teflon-lined stainless steel autoclave at 120 ℃ for 24 h. The

259 Zn-Cr-LDH/g-C_3N_4 product was finally obtained by collecting and drying the
260 precipitates from the autoclave. For constructing LDH/g-C_3N_4 photocatalysts with a
261 better 2D/2D morphology, Wu et al. [54] used urea and NH_4F instead of NaOH
262 alkaline liquor in the hydrothermal synthesis of Co-Al-LDH/O-doped g-C_3N_4. In this
263 process, the hydrolysis of urea was utilized to precipitate Co^{2+} and Al^{3+}, which
264 avoided the unevenness of LDH size resulting from the nonuniform precipitant
265 distribution and reaction rate. Urea broke down into NH_3 and CO_2 by hydrolysis. The
266 generated NH_3 increased the pH value of reaction mixture, while the release of CO_2
267 played a role of agitation. Thus, homogeneous precipitation of Co-Al-LDH flakes
268 gradually occurred, and the products were of high purity and uniform size.
269 Considering the difficulty in recycling powder photocatalysts from aqueous solutions
270 in practical applications, Yazdani et al. [84] fabricated a Ni-Ti-LDH/g-C_3N_4
271 heterojunction film by hydrothermal method and used it as a fix-bed photoreactor. In
272 their experiments, g-C_3N_4 film was first synthesized on a quartz glass substrate via
273 thermal polymerization, and then the g-C_3N_4-covered substrate was further used to
274 load Ni-Ti-LDH film by hydrothermal treatment. The formation of Ni-Ti-LDH was
275 achieved by precipitation through urea hydrolysis. Layered structure of LDH and
276 g-C_3N_4 makes them suitable for constructing 2D photocatalytic films. Using
277 immobilized LDH/g-C_3N_4 photocatalyst may benefit its practical applications in
278 aqueous solutions.
279

3.4. Solvothermal method

Solvothermal method is further developed from hydrothermal method. It uses organic solvents as reaction media. Despite many advantages of hydrothermal method, it is limited in synthesizing some non-oxides (e.g., carbides, nitrides, and phosphides) as the reactants and products may react with water, hydrolyze, or be unstable in water [85]. Using nonaqueous solvents can help to run these reactions successfully. Additionally, many properties of organic solvent (e.g., density, viscosity, and surface tension) vary a lot under high-pressure condition, which can provide special media for many chemical reactions [86]. At the same temperature, the gas pressure in solvothermal system can reach a higher level compared with that in hydrothermal system due to the lower boiling point of some organic solvents, and the high pressure favors the product crystallization [87]. For constructing LDH/g-C_3N_4 heterostructure, organic solvent can improve the dispersity of reaction precursors (e.g., g-C_3N_4 suspension), which increases the chemical reactivity and facilitates the construction of 2D/2D structure. Considering the advantages, solvothermal method was applied for synthesizing LDH/g-C_3N_4 photocatalysts in many studies.

Zhang et al. [88] synthesized Zn-Al-LDH/g-C_3N_4 composites by solvothermal method. In their experiments, ethylene glycol (EG) served as the reaction medium (Fig. 5). The g-C_3N_4 was prepared by calcining urea and suspended in EG with NaOH. Metal salts were added into another EG. The two EG suspensions were then mixed for the solvothermal treatment. According to the TEM observation, g-C_3N_4 sheets were well dispersed in EG and the Zn-Al-LDH/g-C_3N_4 products exhibited a satisfactory

302 layered structure. Additionally, due to the intercalation of EG in the solvothermal
303 reaction, the interlayer distance of Zn-Al-LDH (1.03 nm) was found larger than that
304 of conventional LDHs intercalated with carbonate (0.73 nm). A relatively large
305 interlayer space can provide more space for reactant diffusion and more active sites
306 for photocatalytic reaction, which helps to increase the photocatalytic efficiency [89,
307 90]. Shakeel et al. [91] used a mixed solvent of water and methanol for constructing
308 Ni-Mn-LDH/g-C_3N_4 composite. To obtain a stable g-C_3N_4 nanosheet suspension, the
309 g-C_3N_4 was ultrasonically treated in the mixed solvent before being transferred to the
310 solvothermal reactor. Similar operation was performed with a mixed solvent of water
311 and dimethylformamide (DMF) by Arif et al. [92] in synthesizing Co-Fe-LDH/g-C_3N_4
312 composite. With the assistance of these organic solvents, the dispersity of g-C_3N_4
313 sheets was greatly improved, which contributed to the synthesis of products with high
314 quality.
315
316 *3.5. Calcination method*
317 Calcination is a thermal treatment process in which a substance is heated to lose
318 water or undergo redox reactions. This method is applied for synthesizing calcined
319 LDH/g-C_3N_4 composites. In the synthesis process, LDHs are used as precursors and
320 calcined to form mixed metal oxides (MMOs) via topological transformation [93, 94].
321 The resulting MMOs can be highly dispersed and have a good thermal stability. Due
322 to the formation of metal oxides with higher porosity and specific surface area, the
323 photocatalytic activity can be further improved [95]. Additionally, the calcination of

LDHs may generate spinels that can help to increase the harvesting ability for visible light [96, 97]. According to the available literature, there are three calcination strategies to obtain calcined LDH/g-C_3N_4 composites. The first way is directly calcining prepared LDH/g-C_3N_4 composites [98]. The second method is calcining LDH to MMO, followed by a secondary calcination of the mixture of MMO and g-C_3N_4 raw material [60]. The third approach is calcining the mixture of LDH and g-C_3N_4 raw material together, and this method was more widely used [96, 97, 99, 100]. Fig. 6 illustrates the synthesis of calcined Zn-Fe-LDH/g-C_3N_4 composites through calcining the mixture of Zn-Fe-LDH and melamine together by Di et al. [97]. In the experiment, Zn-Fe-LDH was first synthesized by hydrothermal treatment. Urea hydrolysis was utilized to achieve homogeneous precipitation of Zn^{2+} and Fe^{3+}. Melamine simultaneously underwent the hydrothermal treatment to dissolve and recrystallize after cooling down. The resulting precipitates were then calcined at 550 ℃ to produce the calcined Zn-Fe-LDH/g-C_3N_4 composites. The calcination temperature was relatively higher than that in directly calcining prepared LDH/g-C_3N_4 composites (300 ℃), because the synthesis of g-C_3N_4 needed to be simultaneously accomplished during the topological transformation of LDH to MMO [98]. An attractive property of LDHs is the structural memory effect that many LDH-derived MMOs generated at moderate calcination temperature (generally below 500 ℃) can reconstruct the LDHs by being added to the solution that contains desired anions [101, 102]. This property is conducive to LDHs as adsorbents for removing anionic pollutants from wastewater [93]. However, the memory effect should be abandoned in

346 order to make full use of the photocatalytic capacity of calcined LDHs, as the
347 formation of spinels at high calcination temperature will destroy the structural
348 memory effect [103]. For example, Mg-Al-LDH would generate $MgAl_2O_4$ spinel at a
349 calcination temperature over 600 ℃ [104]. Therefore, it is important to control the
350 calcination temperature when synthesizing calcined LDH/g-C_3N_4 composites for
351 photocatalytic applications.
352
353 **4. Applications of LDH/g-C_3N_4 photocatalytic systems**
354 Rational design of 2D/2D structure can considerably enhance the performance of
355 LDH/g-C_3N_4 photocatalysts, which enables them to be widely used for energy and
356 environmental applications based on solar photocatalysis. The photocatalytic
357 applications mainly involve hydrogen production from water splitting, CO_2 reduction,
358 and organic pollutant degradation. The performance and mechanism of various
359 LDH/g-C_3N_4 photocatalysts are reviewed and discussed in this section.
360
361 *4.1. LDH/g-C_3N_4 binary photocatalysts*
362 According to available literature, divalent cations including Co^{2+}, Mg^{2+}, Ni^{2+},
363 and Zn^{2+}, and trivalent cations including Al^{3+}, Cr^{3+}, Fe^{3+}, Mn^{3+}, and Ti^{3+} were used to
364 construct LDH/g-C_3N_4 binary photocatalysts (Table 1). These LDH/g-C_3N_4
365 photocatalysts with improved photocatalytic activity were explored for solar energy
366 conversion and pollution abatement. Nayak et al. [73] fabricated Ni-Fe-LDH/g-C_3N_4
367 composites with various g-C_3N_4 content (2, 5, 8, 10, 12, and 15 wt%, denoted as

CNLDH2, CNLDH5, CNLDH8, CNLDH10, CNLDH12, and CNLDH15 by the authors, respectively) and applied them for water splitting. Fig. 7a and 7b showed the evolution amount of H_2 and O_2 with different photocatalysts during two-hour irradiation process with visible light. The CNLDH10 composite presented the highest photocatalytic performance for water splitting and the evolution amounts of H_2 and O_2 were 1488 and 886 μmol/g, respectively. The combination of Ni-Fe-LDH and 10 wt% g-C_3N_4 greatly enhanced water splitting efficiency compared with that by only Ni-Fe-LDH or g-C_3N_4. The reduced electron-hole recombination mainly contributed to the result. According to experimental results, the photoluminescence (PL) intensity was negatively related to photocatalytic activity (Fig. 7c). The PL was excited when the electrons and holes recombined, thus the PL spectra suggested that coupling Ni-Fe-LDH and g-C_3N_4 could efficiently separate photoinduced charge carriers and decrease their recombination. In the water splitting process, both Ni-Fe-LDH and g-C_3N_4 could produce electron-hole pairs with visible light irradiation. As the conduction band (CB) edge potential of g-C_3N_4 is more negative than that of Ni-Fe-LDH, the photoinduced electrons on g-C_3N_4 could move to the CB of Ni-Fe-LDH. The electrons (e^-) on the CB of Ni-Fe-LDH were captured by H^+ to generate H_2. Similarly, the holes (h^+) on the valence band (VB) of Ni-Fe-LDH could move to the VB of g-C_3N_4 where the holes oxidized H_2O to form O_2 (Fig. 7d). The photocatalytic process can be explained with the following equations:

$$\text{LDH/g-}C_3N_4 + h\nu \rightarrow \text{LDH/g-}C_3N_4\ (h^+ + e^-) \quad (1)$$

$$\text{LDH/g-}C_3N_4\ (h^+ + e^-) \rightarrow \text{LDH}\ (e^-)\ /\text{g-}C_3N_4\ (h^+) \quad (2)$$

$2H^+ + 2e^- \rightarrow H_2$ (3)

$2H_2O + 4\ h^+ \rightarrow O_2 + 4H^+$ (4)

Apart from being directly used as powder photocatalysts, LDH/g-C_3N_4 composites have also been studied as electrode materials of photoelectrochemical cell (PEC), which can convert solar energy to electric energy for water splitting. The hydrogen and oxygen evolve at the cathode and anode, respectively. Water splitting by PEC can utilize electrode as the photocatalyst support, which simplifies the separation of photocatalyst from water and favors the recycling of photocatalyst. Additionally, the electron-hole recombination can be suppressed by bias voltage. Arif et al. [92] constructed Co-Fe-LDH/g-C_3N_4 composite and used it as both the anode and the cathode in a two-electrode electrolyzer for overall water splitting. Their results suggested that the Co-Fe-LDH/g-C_3N_4 composite could enhance the current density at a lower over potential compared with pristine Co-Fe-LDH and g-C_3N_4. The improved photoelectrocatalytic performance in water splitting mainly resulted from the suppressed electron-hole recombination in Co-Fe-LDH/g-C_3N_4 and its 2D/2D porous structure that provided higher active surface area for gas penetration and release. These examples both demonstrate that LDH/g-C_3N_4 composites can display a higher photocatalytic performance in water splitting through the construction of 2D/2D structure and rational ratio control, and the enhanced performance is mainly due to the decreased electron-hole recombination in the heterojunction.

Tonda et al. [53] constructed 2D/2D Ni-Al-LDH/g-C_3N_4 composites with various weight percentages of Ni-Al-LDH (5, 10, 15, and 20 wt%, denoted as CNLDH-5,

412 CNLDH-10, CNLDH-15, and CNLDH-20 by the authors, respectively) for realizing
413 high-efficient photocatalytic CO_2 reduction. The TEM images showed successful
414 2D/2D assembly and intimate interface of Ni-Al-LDH/g-C_3N_4 composite (Fig. 8a-c).
415 The results of photocatalytic experiments showed that CNLDH-10 presented the
416 highest activity to reduce CO_2 to CO, H_2, and O_2 (Fig. 8d, e, and f). The optimal
417 evolution rate of CO with CNLDH-10 was reported to be 8.2 μmol/h/g, and this value
418 was much higher than that with only Ni-Al-LDH (0.92 μmol/h/g) and g-C_3N_4 (1.56
419 μmol/h/g). An experiment by using physical mixture of Ni-Al-LDH (10 wt%) and
420 g-C_3N_4 as the photocatalyst was carried out for comparison, and the evolution rate of
421 CO was only 2.84 μmol/h/g. This result demonstrated the importance of intimate
422 contact between LDH and g-C_3N_4 in achieving high photocatalytic performance with
423 LDH/g-C_3N_4 composites. In the photocatalytic mechanism study, CNLDH-10 showed
424 the lowest PL intensity and the highest transient photocurrent responses (Fig. 8g and
425 h), which was consistent with its high photocatalytic performance in CO_2 reduction.
426 The possible photocatalytic mechanism for CO_2 reduction by Ni-Al-LDH/g-C_3N_4
427 photocatalyst was proposed and illustrated as shown in Fig. 8i. Both Ni-Al-LDH and
428 g-C_3N_4 could produce electrons and holes under the irradiation of visible light. The
429 electrons on the CB of g-C_3N_4 could transfer to the CB of Ni-Al-LDH, while the holes
430 on the VB of Ni-Al-LDH could move to the VB of g-C_3N_4. The accumulated
431 electrons on the CB of Ni-Al-LDH reduced CO_2 to CO. The reduction process of CO_2
432 was described by the following equation and redox potential (vs. NHE, at pH 7.00):

433 $$CO_2 + 2H^+ + 2e^- \rightarrow CO + H_2O,\ E = -0.53\ V \quad (5)$$

Except being reduced to CO for renewable fuels, CO_2 may also be reduced to HCOOH, HCHO, CH_3OH, and CH_4 with different redox potential (vs. NHE, at pH 7.00) [107]:

$$CO_2 + 2H^+ + 2e^- \rightarrow HCOOH,\ E = -0.61\ V \quad (6)$$

$$CO_2 + 4H^+ + 4e^- \rightarrow HCHO + H_2O,\ E = -0.48\ V \quad (7)$$

$$CO_2 + 6H^+ + 6e^- \rightarrow CH_3OH + H_2O,\ E = -0.38\ V \quad (8)$$

$$CO_2 + 8H^+ + 8e^- \rightarrow CH_4 + 2H_2O,\ E = -0.24\ V \quad (9)$$

For example, Hong et al. [72] constructed Mg-Al-LDH/g-C_3N_4 photocatalysts and used them for reducing CO_2 to CH_4. If this technique can be successfully applied in practical engineering, both the global warming and energy crisis will be alleviated.

Salehi et al. [106] synthesized Ni-Al-LDH/g-C_3N_4 composites with various weight percentages of g-C_3N_4 (10, 20, 30, 40, and 50 wt%, denoted as g-C_3N_4-10@NiAl-LDH, g-C_3N_4-20@NiAl-LDH, g-C_3N_4-30@NiAl-LDH, g-C_3N_4-40@NiAl-LDH, and g-C_3N_4-50@NiAl-LDH by the authors, respectively) and studied their photocatalytic activity for removing rhodamine B (RhB) and methyl orange (MO) in wastewater. Fig. 9a showed the typical 2D/2D structure of the synthesized Ni-Al-LDH/g-C_3N_4 composites. The g-C_3N_4-40@NiAl-LDH displayed the highest photocatalytic performance in degrading RhB (Fig. 9b), while the g-C_3N_4-20@NiAl-LDH showed the highest photocatalytic performance in degrading MO (Fig. 9c). With the optimal photocatalyst, the removal rates of RhB and MO both reached 93% after visible light irradiation of 240 and 180 min, respectively. For elucidating the photocatalytic degradation mechanism, p-benzoquinone (BQ, O_2^-

scavenger), isopropanol (IPA, ·OH scavenger), and Na_2-EDTA (h^+ scavenger) were used to identify important oxidative species in the Ni-Al-LDH/g-C_3N_4 photocatalytic systems. The significant inhibition of dye degradation with the incorporation of isopropanol and Na_2-EDTA implied that the generation of ·OH and h^+ mainly contributed to the dye degradation (Fig. 9d). As illustrated in Fig. 9e, ·OH could be generated when O_2 was reduced by the enriched electrons on the CB of Ni-Al-LDH. The generated ·OH and accumulated h^+ on the VB of g-C_3N_4 contributed to the oxidative degradation of RhB and MO. Additionally, h^+ could also lead to the formation of ·OH. Related reactions are expressed by the following equations:

$$e^- + O_2 \rightarrow \cdot O_2^- \quad (6)$$

$$2\ O_2^- + 2H^+ \rightarrow H_2O_2 + O_2 \quad (7)$$

$$H_2O_2 + e^- \rightarrow \cdot OH + OH^- \quad (8)$$

$$h^+ + H_2O \rightarrow H^+ + \cdot OH \quad (9)$$

$$\cdot OH + RhB \rightarrow \text{degradation products} \quad (10)$$

$$\cdot OH + MO \rightarrow \text{degradation products} \quad (11)$$

$$h^+ + RhB \rightarrow \text{degradation products} \quad (12)$$

$$h^+ + MO \rightarrow \text{degradation products} \quad (13)$$

In the experiments that assessed the photocatalytic performance of LDH/g-C_3N_4 composites for removing organic pollutants, organic dyes were generally selected as model pollutants due to the relatively obvious experimental phenomenon and convenient measurement. Additionally, some antibiotics and endocrine disruptors were targeted in the degradation experiments [54, 55]. Zhang et al. [88] fabricated

Zn-Al-LDH/g-C_3N_4 composites and applied them to degrade methylene blue (MB). In the experiments, Zn-Al-LDH/g-C_3N_4 photocatalyst completely removed the MB under the irradiation of ultraviolet (UV) light for 60 min, while g-C_3N_4 and Zn-Al-LDH could only remove 55.0% and 21.0% MB under the same conditions, respectively. This demonstrated the improved photocatalytic activity after the combination of Zn-Al-LDH and g-C_3N_4. However, commercial ZnO photocatalyst only took 20 min to completely remove the MB under UV light irradiation. Under the irradiation of visible light, the Zn-Al-LDH/g-C_3N_4 photocatalyst removed 100% MB within 240 min, but only 27.2% MB was removed by the commercial ZnO photocatalyst under the same conditions. The higher performance of Zn-Al-LDH/g-C_3N_4 photocatalyst under visible light made it more competitive in solar photocatalysis. Considering the practical applications, Yazdani et al. [84] constructed Ni-Ti-LDH/g-C_3N_4 films on quartz glass substrates and used them for photocatalytic degradation of MO. The films were placed in a reactor where the MO solution was circulated over the film surface under visible light irradiation. After a single run, the films could be directly taken out, washed, and dried for the next run. Immobilizing Ni-Ti-LDH/g-C_3N_4 photocatalyst on the film simplified the process of recycling photocatalysts from aqueous solutions compared with using powder photocatalysts, which might be beneficial for the practical applications.

4.2. LDH/g-C_3N_4/X ternary photocatalysts

Though coupling LDH and g-C_3N_4 can increase the electron-hole separation, the charge carriers on some LDH/g-C_3N_4 photocatalysts are difficult to further transfer and participate in redox reactions [108]. Therefore, constructing LDH/g-C_3N_4/X ternary photocatalysts is considered, where X represents other semiconductor or noble metal. This strategy is expected to not only facilitate the charge carrier transfer at the interface of LDH and g-C_3N_4, but also improve the harvesting ability for visible light. According to available literature, Ag and reduced graphene oxide (RGO) were primarily used to realize these goals [108-111].

Tonda and Jo [111] incorporated 1 wt% Ag nanoparticles into Ni-Al-LDH/g-C_3H_4 composites with various weight percentages of Ni-Al-LDH (5, 10, 15, and 20 wt%, denoted as ALDHCN-5, ALDHCN-10, ALDHCN-15, and ALDHCN-20 by the authors, respectively) and studied their photocatalytic performance in degrading RhB and 4-chlorophenol (4-CP). In their study, the Ni-Al-LDH/g-C_3N_4 composites were first fabricated through hydrothermal method, and then the composites were decorated with Ag nanoparticles via a photo-reduction process to form Ni-Al-LDH/g-C_3N_4/Ag hybrids (Fig. 10a). The deposition of Ag nanoparticles on Ni-Al-LDH/g-C_3H_4 was clearly observed with TEM image (Fig. 10b). The combination of Ni-Al-LDH and g-C_3H_4 greatly increased the photocatalytic activity in degrading both RhB and 4-CP, while the incorporation of Ag nanoparticles further enhanced the photocatalytic performance (Fig. 10c and d). In the mechanism study, the photocatalytic activity of ALDHCN-15 was significantly inhibited in the

520 presence of ammonium oxalate (AO, h^+ scavenger), benzoquinone (BZQ, $\cdot O_2^-$
521 scavenger), tert-butanol (TBA, $\cdot OH$ scavenger). The order of inhibiting ability was
522 BZQ > TBA > AO (Fig. 10e). This result demonstrated that $\cdot O_2^-$ and $\cdot OH$ were the
523 main active species that accounted for the pollutant degradation. The generation
524 of $\cdot OH$ during the photocatalytic process was further confirmed by $\cdot OH$ trapping PL
525 spectra in terephthalic acid solution (Fig. 10f). The possible photocatalytic mechanism
526 of Ni-Al-LDH/g-C_3N_4/Ag composite was illustrated in Fig. 10g. Both Ni-Al-LDH and
527 g-C_3N_4 could generate electron-hole pairs under visible light. Because the CB of
528 g-C_3N_4 (−1.32 eV) is more negative than that of Ni-Al-LDH (−0.72 eV), the electrons
529 on the CB of g-C_3N_4 could move to the CB of Ni-Al-LDH. Similarly, the holes on the
530 VB of Ni-Al-LDH could transfer to the VB of g-C_3N_4. This facilitated the
531 electron-hole separation. The surface Ag nanoparticles on the composites were
532 excellent electron trappers, which could transfer electrons from the CB of both
533 Ni-Al-LDH and g-C_3N_4. Therefore, the electron-hole separation efficiency was further
534 enhanced, contributing to the higher photocatalytic performance. Nayak and Parida
535 [109] added Ag@Ag_3PO_4 component into Ni-Fe-LDH/g-C_3N_4 to improve the
536 performance for photocatalytic Cr(VI) reduction and phenol degradation. It was
537 reported that Ag nanoparticles could induce surface plasmon resonance, in which free
538 electrons on the surface of Ag nanoparticles oscillated collectively under the light
539 irradiation. The plasmon resonance improved the light harvesting capacity and thus
540 enhanced the photocatalytic Cr(VI) reduction and phenol degradation. This offered

another mechanism by which Ag nanoparticles promote the performance of LDH/g-C_3N_4 photocatalyst.

Jo and Tonda [108] fabricated Co-Al-LDH/g-C_3N_4/RGO composites with 1 wt% RGO and various weight percentages of Co-Al-LDH (5, 10, 15, and 20 wt%, denoted as LCR-5, LCR-10, LCR-15, and LCR-20 by the authors, respectively) and applied them for photocatalytic degradation of Congo red (CR) and tetracycline (TC). The composites were synthesized by adding RGO suspension into the mixture of Co-Al-LDH and g-C_3N_4 before the hydrothermal reaction (Fig. 11a). The TEM image of LCR-15 showed a typical 2D/2D/2D structure. The incorporation of RGO considerably improved the photocatalytic activity of Co-Al-LDH/g-C_3N_4 composites in degrading CR and TC, and LCR-15 exhibited the highest photocatalytic performance for degrading both the pollutants. Due to the generation of intermediate products, the decoloration of CR is generally not equal to that the pollutant has been completely mineralized into CO_2 and H_2O. Fig. 11e showed the removal of total organic carbon (TOC) by LCR-15 in removing CR, which suggested the pollutant mineralization by the photocatalytic process. The LCR-15 photocatalyst could remove 79% TOC from CR solution under visible light for 30 min. The high photocatalytic activity of Co-Al-LDH/g-C_3N_4/RGO composites could be partly ascribed to the enhanced light harvesting ability due to the RGO incorporation. As shown in the UV-vis diffuse reflection spectra (DRS, Fig. 11f), the presence of RGO increased the absorption capacity of Co-Al-LDH/g-C_3N_4/RGO for visible light. Additionally, because of the conductivity of RGO, the generated electrons on the CB of both

563 Co-Al-LDH and g-C_3N_4 could transfer along the RGO network, further enhancing the
564 electron-hole separation for degrading CR and TC (Fig. 11g). Nayak and Parida [110]
565 added N-doped RGO into Ni-Fe-LDH/g-C_3N_4 to increase the photocatalytic activity
566 in degrading RhB and phenol, as well as producing H_2 and O_2. Doping nitrogen on the
567 RGO networks facilitated the charge transfer between adjacent carbon atoms. The
568 direct coupling of N-doped RGO and transition-metal atom sites on Ni-Fe-LDH
569 accelerated the charge transfer at the interface of LDH/g-C_3N_4. These attempts
570 provided valuable experience for using RGO to further promote charge transfer at the
571 interface of LDH/g-C_3N_4 and the absorption capacity for visible light.
572
573 *4.3. Calcined LDH/g-C_3N_4 photocatalysts*
574 Calcining LDH/g-C_3N_4 composites or using LDHs as precursors can fabricate
575 calcined LDH/g-C_3N_4 with higher surface area and better photocatalytic activity [60,
576 94, 96-100]. The topological transformation of homogeneous LDHs ensures the
577 formation of highly dispersed MMOs on g-C_3N_4. Besides metal oxides, the
578 calcination of LDHs may generate spinels which present smaller band gap than metal
579 oxides and can serve as light sensitizer to increase the harvesting ability for visible
580 light [96, 97].
581 Lan et al. [100] fabricated some calcined Zn-In-LDH/g-C_3N_4 composites from
582 different weight ratios of melamine and Zn-In-LDH (1:1, 3:1, and 5:1, denoted as
583 1-MMO/C_3N_4, 3-MMO/C_3N_4, and 5-MMO/C_3N_4 by the authors, respectively). These
584 composites were applied for the degradation of RhB. Fig. 12a showed the 2D layered

structure of the calcined Zn-In-LDH/g-C_3N_4 composite. The XRD patterns suggested that ZnO had a higher crystallinity than In_2O_3 in the calcined Zn-In-LDH/g-C_3N_4 composites (Fig. 12b). The 3-MMO/C_3N_4 showed the highest photocatalytic activity for RhB degradation, showing a complete removal of RhB within 60 min (Fig. 12c). Additionally, the degradation efficiency of RhB was still over 95% after the 3-MMO/C_3N_4 was recycled for eight times, which indicated the stability of photocatalyst (Fig. 12d). The higher photocatalytic performance of calcined Zn-In-LDH/g-C_3N_4 composite was attributed to higher photocurrent response (Fig. 12e), and the generation of more $\cdot O_2^-$ and $\cdot OH$ (Fig. 12f and g). The possible mechanism for the carrier transfer was illustrated in Fig. 12h. Under visible light irradiation, many charge carriers were generated on the g-C_3N_4 and In_2O_3. The transfer of electrons and holes through the heterojunction interface separated the charge carriers and enriched holes on the VB of g-C_3N_4 and electrons on the CB of In_2O_3. The ZnO further improved the charge separation efficiency because of the excellent electron mobility of ZnO. The electrons could be accepted by oxygen to generate $\cdot O_2^-$ and $\cdot OH$, and these strong oxidants decomposed the RhB. Shi et al. [60] constructed 2D/2D calcined Mg-Fe-LDH/g-C_3N_4 photocatalyst and achieved an improved H_2 production under the irradiation of visible light. In their experiments, it was found that the CB position was tunable and the product with a smaller CB potential could be obtained with a more addition amount of calcined Mg-Fe-LDH. The result provided valuable information for tuning band structure of LDH/g-C_3N_4 photocatalyst to meet the demands in different applications.

607 Di et al. [97] synthesized several kinds of calcined Zn-Fe-LDH/g-C_3N_4
608 composites with various weight percentages of g-C_3N_4 (0.5, 1.0, 5.0, 70, and 90,
609 denoted as CNZF-0.5, CNZF-1.0, CNZF-5.0, CNZF-70, and CNZF-90 by the authors,
610 respectively) and explored their photocatalytic activity in degrading ibuprofen (IBF)
611 and sulfadiazine (SDZ). The high-resolution TEM images showed the intimate
612 face-to-face contact between calcined Zn-Fe-LDH and g-C_3N_4 (Fig. 13a and b). The
613 characteristic diffractions of ZnO and $ZnFe_2O_4$ were observed with the XRD pattern
614 of calcined Zn-Fe-LDH (Fig. 13c). The CNZF-1.0 and CNZF-90 exhibited the best
615 photocatalytic performance among the prepared photocatalysts in the IBF and SDZ
616 degradation process, respectively (Fig. 13d and e). Different scavengers for h^+
617 (Na_2-EDTA), O_2^- (BQ), and ·OH (IPA) were used in the photocatalytic systems to
618 identify the main oxidative species that accounted for the pollutant degradation. It was
619 found that h^+ mainly contributed to the degradation of IBF by CNZF-1.0
620 photocatalyst (Fig. 13f), and the degradation of SDZ by CNZF-90 mainly resulted
621 from the generation of ·OH (Fig. 13g). A Z-scheme charge transfer mechanism was
622 proposed for explaining the improved photocatalytic performance of calcined
623 Zn-Fe-LDH/g-C_3N_4 composites (Fig. 13h). The authors did not directly present the
624 inference process about the Z-scheme charge transfer mechanism. However, it was
625 indicated by their experimental results. The photoinduced generation of ·OH on
626 Zn-Fe-LDH/g-C_3N_4 was ascertained by electron paramagnetic resonance (EPR)
627 spectra (Fig. 13h). The redox potential needed for ·OH generation was more positive
628 than the VB potential of g-C_3N_4. If the photoinduced h^+ accumulated on VB of

629 g-C_3N_4, the resulting redox ability would be insufficient for $\cdot OH$ generation [112].
630 Therefore, it should be a Z-scheme charge transfer mechanism. Under visible light
631 irradiation, both g-C_3N_4 and ZnO in the heterojunction could generate electron-hole
632 pairs. The generated electrons on the CB of ZnO could move to the VB of g-C_3N_4 and
633 recombine with the holes generated there. This resulted in the electron-hole separation,
634 and the accumulation of electrons on the CB of g-C_3N_4 and holes on the VB of ZnO
635 contributed to the removal of IBF and SDZ. The $ZnFe_2O_4$ spinel phase played a role
636 of light sensitizer, which enhanced the light harvesting and charge carrier generation.
637 Similar role of $ZnCr_2O_4$ spinel phase in the calcined Zn-Cr-LDH/g-C_3N_4
638 photocatalyst was reported by Patnaik et al. [96]. Because of smaller band gap of
639 $ZnCr_2O_4$ (1.5 eV) than that of ZnO (3.2 eV), $ZnCr_2O_4$ could harvest visible light and
640 sensitize ZnO to promote the photocatalytic performance. These studies suggested
641 that the formation of spinel phase in calcined LDH/g-C_3N_4 could increase
642 photocatalytic performance by enhancing the absorption of visible light.
643

644 **5. Conclusion and outlook**

645 In summary, constructing 2D/2D LDH/g-C_3N_4 heterojunction is an effective
646 approach to achieve high performance in solar photocatalysis for pollution abatement
647 and energy conversion. The planar structure and face-to-face contact of LDH and
648 g-C_3N_4 can greatly facilitate the separation and transfer of photoinduced charge
649 carriers, thus improving the photocatalytic performance. Many synthesis methods
650 including electrostatic self-assembly, in-situ coprecipitation, hydrothermal method,

651 solvothermal method, and calcination method have been developed for constructing
652 LDH/g-C_3N_4 heterojunction with desired 2D/2D structure and rational band gaps. The
653 synergetic effect of LDH and g-C_3N_4 has contributed to high photocatalytic
654 performance in hydrogen production, CO_2 reduction, and organic pollutant
655 degradation. Fabricating LDH/g-C_3N_4/X ternary photocatalysts and calcined
656 LDH/g-C_3N_4 composites is effective for further improving and optimizing the
657 photocatalytic performance. The following points may be considered in future
658 research:

659 (1) Increasing the harvesting ability for visible light and even near infrared light
660 that accounts for more than 50% of solar irradiation. Though LDH/g-C_3N_4
661 photocatalysts can function under visible light, the harvesting ability for sun light may
662 be further improved through surface sensitization, doping element, band gap
663 adjustment, etc.

664 (2) Matching the CB (or VB) potential of LDH/g-C_3N_4 photocatalysts with the
665 redox potential for specific photocatalytic reaction. Since the band structure of
666 LDH/g-C_3N_4 is tunable, it is possible to adjust the CB (or VB) position to provide
667 high redox potential for various photocatalytic reactions. However, the accurate
668 adjustment method needs further study.

669 (3) Going deep into the transfer mechanism of charge carriers. Better
670 understanding of the mechanism is helpful for seeking more LDH materials that can
671 combine with g-C_3N_4 to achieve better photocatalytic performance.

672 (4) Photocatalytic reaction mechanisms. How the reactants contact and interact
673 with the LDH/g-C_3N_4 photocatalysts, and the effects of photocatalyst properties (e.g.,
674 size and porosity) on the photocatalytic activity need to be further illuminated.
675 (5) Constructing ultrathin 2D/2D structure. Some studies have proposed the
676 ultrathin LDH and g-C_3N_4 as photocatalysts [113-115]. It is also possible to construct
677 ultrathin LDH/g-C_3N_4 heterostructure that will enable faster carrier transfer due to the
678 further shortened transfer distance from inner to surface and reduced electron-hole
679 recombination in the bulk phase.
680 (6) Application expansion. Current uses of LDH/g-C_3N_4 composites mainly
681 target at photocatalytic water splitting and organic pollutant degradation. The
682 application for CO_2 reduction is relatively fewer. Existing and new LDH/g-C_3N_4
683 photocatalysts may also be explored for applications in degradation of other more
684 organic pollutants, Cr(VI) reduction, and nitrogen fixation. Simultaneously, the
685 photocatalytic conditions should be recorded and optimized in different applications.
686 (7) Practical engineering applications. Most studies were conducted under
687 laboratory conditions. Considering the practical applications, the design of applicable
688 reaction systems for LDH/g-C_3N_4 photocatalysts is required.
689

690 **Acknowledgements**

691 This work was supported by National Natural Science Foundation of China
692 (51378190, 51508177, 51521006, 51579095, 51709101), the Program for Changjiang
693 Scholars and Innovative Research Team in University (IRT-13R17).

694

References

[1] Song B, Zeng G, Gong J, Liang J, Xu P, Liu Z, et al. Evaluation methods for assessing effectiveness of in situ remediation of soil and sediment contaminated with organic pollutants and heavy metals. Environment International. 2017;105:43-55.

[2] Gong JL, Wang B, Zeng GM, Yang CP, Niu CG, Niu QY, et al. Removal of cationic dyes from aqueous solution using magnetic multi-wall carbon nanotube nanocomposite as adsorbent. Journal of Hazardous Materials. 2009;164:1517-1522.

[3] Tang X, Zeng G, Fan C, Zhou M, Tang L, Zhu J, et al. Chromosomal expression of CadR on Pseudomonas aeruginosa for the removal of Cd(II) from aqueous solutions. Science of The Total Environment. 2018;636:1355-1361.

[4] Ye S, Zeng G, Wu H, Zhang C, Liang J, Dai J, et al. Co-occurrence and interactions of pollutants, and their impacts on soil remediation—A review. Critical Reviews in Environmental Science and Technology. 2017;47:1528-1553.

[5] Song B, Chen M, Ye S, Xu P, Zeng G, Gong J, et al. Effects of multi-walled carbon nanotubes on metabolic function of the microbial community in riverine sediment contaminated with phenanthrene. Carbon. 2019;144:1-7.

[6] Jiang D, Chen M, Wang H, Zeng G, Huang D, Cheng M, et al. The application of different typological and structural MOFs-based materials for the dyes adsorption. Coordination Chemistry Reviews. 2019;380:471-483.

[7] Kabir E, Kumar P, Kumar S, Adelodun AA, Kim K-H. Solar energy: Potential and future prospects. Renewable and Sustainable Energy Reviews. 2018;82:894-900.

[8] Borges ME, Sierra M, Cuevas E, Garc á RD, Esparza P. Photocatalysis with solar

717 energy: Sunlight-responsive photocatalyst based on TiO_2 loaded on a natural material
718 for wastewater treatment. Solar Energy. 2016;135:527-535.
719 [9] Spasiano D, Marotta R, Malato S, Fernandez-Ibañez P, Di Somma I. Solar
720 photocatalysis: Materials, reactors, some commercial, and pre-industrialized
721 applications. A comprehensive approach. Applied Catalysis B: Environmental.
722 2015;170-171:90-123.
723 [10] Yang Y, Zhang C, Lai C, Zeng G, Huang D, Cheng M, et al. BiOX (X = Cl, Br, I)
724 photocatalytic nanomaterials: Applications for fuels and environmental management.
725 Advances in Colloid and Interface Science. 2018;254:76-93.
726 [11] Lai C, Zhang M, Li B, Huang D, Zeng G, Qin L, et al. Fabrication of CuS/$BiVO_4$
727 (0 4 0) binary heterojunction photocatalysts with enhanced photocatalytic activity for
728 Ciprofloxacin degradation and mechanism insight. Chemical Engineering Journal.
729 2019;358:891-902.
730 [12] Li B, Lai C, Zeng G, Qin L, Yi H, Huang D, et al. Facile Hydrothermal Synthesis
731 of Z-Scheme $Bi_2Fe_4O_9$/Bi_2WO_6 Heterojunction Photocatalyst with Enhanced Visible
732 Light Photocatalytic Activity. ACS Applied Materials & Interfaces.
733 2018;10:18824-18836.
734 [13] Zhou C, Lai C, Huang D, Zeng G, Zhang C, Cheng M, et al. Highly porous
735 carbon nitride by supramolecular preassembly of monomers for photocatalytic
736 removal of sulfamethazine under visible light driven. Applied Catalysis B:
737 Environmental. 2018;220:202-210.
738 [14] He K, Chen G, Zeng G, Chen A, Huang Z, Shi J, et al. Three-dimensional

graphene supported catalysts for organic dyes degradation. Applied Catalysis B: Environmental. 2018;228:19-28.

[15] Yang D, Zhao X, Zou X, Zhou Z, Jiang Z. Removing Cr (VI) in water via visible-light photocatalytic reduction over Cr-doped $SrTiO_3$ nanoplates. Chemosphere. 2019;215:586-595.

[16] Kretschmer I, Senn AM, Meichtry JM, Custo G, Halac EB, Dillert R, et al. Photocatalytic reduction of Cr(VI) on hematite nanoparticles in the presence of oxalate and citrate. Applied Catalysis B: Environmental. 2019;242:218-226.

[17] Wang T, Sun M, Sun H, Shang J, Wong PK. Efficient Z-scheme visible-light-driven photocatalytic bacterial inactivation by hierarchical MoS_2-encapsulated hydrothermal carbonation carbon core-shell nanospheres. Applied Surface Science. 2019;464:43-52.

[18] Wang W, Li G, An T, Chan DKL, Yu JC, Wong PK. Photocatalytic hydrogen evolution and bacterial inactivation utilizing sonochemical-synthesized g-C_3N_4/red phosphorus hybrid nanosheets as a wide-spectral-responsive photocatalyst: The role of type I band alignment. Applied Catalysis B: Environmental. 2018;238:126-135.

[19] Kandy MM, Gaikar VG. Enhanced photocatalytic reduction of CO_2 using CdS/Mn_2O_3 nanocomposite photocatalysts on porous anodic alumina support with solar concentrators. Renewable Energy. 2019;139:915-923.

[20] Yang X, Hu Z, Yin Q, Shu C, Jiang XF, Zhang J, et al. Water-Soluble Conjugated Molecule for Solar-Driven Hydrogen Evolution from Salt Water. Advanced Functional Materials. ;0:1808156.

761 [21] Dong J, Shi Y, Huang C, Wu Q, Zeng T, Yao W. A New and stable Mo-Mo_2C
762 modified g-C_3N_4 photocatalyst for efficient visible light photocatalytic H_2 production.
763 Applied Catalysis B: Environmental. 2019;243:27-35.
764 [22] Tahir M. Hierarchical 3D VO_2/ZnV_2O_4 microspheres as an excellent visible light
765 photocatalyst for CO2 reduction to solar fuels. Applied Surface Science.
766 2019;467-468:1170-1180.
767 [23] Yang Y, Zeng Z, Zhang C, Huang D, Zeng G, Xiao R, et al. Construction of
768 iodine vacancy-rich BiOI/Ag@AgI Z-scheme heterojunction photocatalysts for
769 visible-light-driven tetracycline degradation: Transformation pathways and
770 mechanism insight. Chemical Engineering Journal. 2018;349:808-821.
771 [24] Zhou C, Lai C, Zhang C, Zeng G, Huang D, Cheng M, et al.
772 Semiconductor/boron nitride composites: Synthesis, properties, and photocatalysis
773 applications. Applied Catalysis B: Environmental. 2018;238:6-18.
774 [25] Ye S, Yan M, Tan X, Liang J, Zeng G, Wu H, et al. Facile assembled
775 biochar-based nanocomposite with improved graphitization for efficient
776 photocatalytic activity driven by visible light. Applied Catalysis B: Environmental.
777 2019;250:78-88.
778 [26] Yi H, Yan M, Huang D, Zeng G, Lai C, Li M, et al. Synergistic effect of artificial
779 enzyme and 2D nano-structured Bi_2WO_6 for eco-friendly and efficient biomimetic
780 photocatalysis. Applied Catalysis B: Environmental. 2019;250:52-62.
781 [27] Ong WJ, Tan LL, Ng YH, Yong ST, Chai SP. Graphitic Carbon Nitride
782 (g-C_3N_4)-Based Photocatalysts for Artificial Photosynthesis and Environmental

783 Remediation: Are We a Step Closer To Achieving Sustainability? Chemical Reviews.
784 2016;116:7159-7329.
785 [28] Kumar S, Karthikeyan S, Lee AF. g-C_3N_4-Based Nanomaterials for Visible
786 Light-Driven Photocatalysis. Catalysts. 2018;8:74.
787 [29] Wang X, Maeda K, Thomas A, Takanabe K, Xin G, Carlsson JM, et al. A
788 metal-free polymeric photocatalyst for hydrogen production from water under
789 visible light. Nature Materials. 2009;8:76-80.
790 [30] Wen J, Xie J, Chen X, Li X. A review on g-C_3N_4-based photocatalysts. Applied
791 Surface Science. 2017;391:72-123.
792 [31] Fu J, Yu J, Jiang C, Cheng B. g-C_3N_4-Based Heterostructured Photocatalysts.
793 Advanced Energy Materials. 2018;8:1701503.
794 [32] Xiong T, Cen W, Zhang Y, Dong F. Bridging the g-C_3N_4 Interlayers for Enhanced
795 Photocatalysis. ACS Catalysis. 2016;6:2462-2472.
796 [33] Mamba G, Mishra AK. Graphitic carbon nitride (g-C_3N_4) nanocomposites: A new
797 and exciting generation of visible light driven photocatalysts for environmental
798 pollution remediation. Applied Catalysis B: Environmental. 2016;198:347-377.
799 [34] Xie L, Ai Z, Zhang M, Sun R, Zhao W. Enhanced Hydrogen Evolution in the
800 Presence of Plasmonic Au-Photo-Sensitized g-C_3N_4 with an Extended Absorption
801 Spectrum from 460 to 640 nm. PLOS ONE. 2016;11:e0161397.
802 [35] Li X, Pi Y, Wu L, Xia Q, Wu J, Li Z, et al. Facilitation of the visible
803 light-induced Fenton-like excitation of H_2O_2 via heterojunction of g-C_3N_4/NH_2-Iron
804 terephthalate metal-organic framework for MB degradation. Applied Catalysis B:

805 Environmental. 2017;202:653-663.

806 [36] Dong F, Li Y, Wang Z, Ho W-K. Enhanced visible light photocatalytic activity
807 and oxidation ability of porous graphene-like g-C_3N_4 nanosheets via thermal
808 exfoliation. Applied Surface Science. 2015;358:393-403.

809 [37] Wang K, Li Q, Liu B, Cheng B, Ho W, Yu J. Sulfur-doped g-C_3N_4 with enhanced
810 photocatalytic CO_2-reduction performance. Applied Catalysis B: Environmental.
811 2015;176-177:44-52.

812 [38] Liu J, Jia Q, Long J, Wang X, Gao Z, Gu Q. Amorphous NiO as co-catalyst for
813 enhanced visible-light-driven hydrogen generation over g-C_3N_4 photocatalyst.
814 Applied Catalysis B: Environmental. 2018;222:35-43.

815 [39] Zhu YP, Ren TZ, Yuan ZY. Mesoporous Phosphorus-Doped g-C_3N_4
816 Nanostructured Flowers with Superior Photocatalytic Hydrogen Evolution
817 Performance. ACS Applied Materials & Interfaces. 2015;7:16850-16856.

818 [40] Yang X, Qian F, Zou G, Li M, Lu J, Li Y, et al. Facile fabrication of acidified
819 g-C_3N_4/g-C_3N_4 hybrids with enhanced photocatalysis performance under visible light
820 irradiation. Applied Catalysis B: Environmental. 2016;193:22-35.

821 [41] Low J, Yu J, Jaroniec M, Wageh S, Al-Ghamdi AA. Heterojunction
822 Photocatalysts. Advanced Materials. 2017;29:1601694.

823 [42] Carrasco JA, Harvey A, Hanlon D, Lloret V, McAteer D, Sanchis-Gual R, et al.
824 Liquid phase exfoliation of carbonate-intercalated layered double hydroxides.
825 Chemical Communications. 2019;55:3315-3318.

826 [43] Li C, Wei M, Evans DG, Duan X. Recent advances for layered double hydroxides

827 (LDHs) materials as catalysts applied in green aqueous media. Catalysis Today.
828 2015;247:163-169.
829 [44] Mohapatra L, Parida K. A review on the recent progress, challenges and
830 perspective of layered double hydroxides as promising photocatalysts. Journal of
831 Materials Chemistry A. 2016;4:10744-10766.
832 [45] Luo B, Liu G, Wang L. Recent advances in 2D materials for photocatalysis.
833 Nanoscale. 2016;8:6904-6920.
834 [46] Zhao Y, Hu H, Yang X, Yan D, Dai Q. Tunable Electronic Transport Properties of
835 2D Layered Double Hydroxide Crystalline Microsheets with Varied Chemical
836 Compositions. Small. 2016;12:4471-4476.
837 [47] Wang Q, O'Hare D. Recent Advances in the Synthesis and Application of
838 Layered Double Hydroxide (LDH) Nanosheets. Chemical Reviews.
839 2012;112:4124-4155.
840 [48] Ong WJ. 2D/2D Graphitic Carbon Nitride ($g\text{-}C_3N_4$) Heterojunction
841 Nanocomposites for Photocatalysis: Why Does Face-to-Face Interface Matter?
842 Frontiers in Materials. 2017;4.
843 [49] Ni J, Xue J, Xie L, Shen J, He G, Chen H. Construction of magnetically separable
844 NiAl LDH/Fe_3O_4–RGO nanocomposites with enhanced photocatalytic performance
845 under visible light. Physical Chemistry Chemical Physics. 2018;20:414-421.
846 [50] Fan G, Li F, Evans DG, Duan X. Catalytic applications of layered double
847 hydroxides: recent advances and perspectives. Chemical Society Reviews.
848 2014;43:7040-7066.

849 [51] Xu ZP, Zhang J, Adebajo MO, Zhang H, Zhou C. Catalytic applications of
850 layered double hydroxides and derivatives. Applied Clay Science. 2011;53:139-150.
851 [52] He S, An Z, Wei M, Evans DG, Duan X. Layered double hydroxide-based
852 catalysts: nanostructure design and catalytic performance. Chemical Communications.
853 2013;49:5912-5920.
854 [53] Tonda S, Kumar S, Bhardwaj M, Yadav P, Ogale S. g-C_3N_4/NiAl-LDH 2D/2D
855 Hybrid Heterojunction for High-Performance Photocatalytic Reduction of CO_2 into
856 Renewable Fuels. ACS Applied Materials & Interfaces. 2018;10:2667-2678.
857 [54] Wu Y, Wang H, Sun Y, Xiao T, Tu W, Yuan X, et al. Photogenerated charge
858 transfer via interfacial internal electric field for significantly improved photocatalysis
859 in direct Z-scheme oxygen-doped carbon nitrogen/CoAl-layered double hydroxide
860 heterojunction. Applied Catalysis B: Environmental. 2018;227:530-540.
861 [55] Abazari R, Mahjoub AR, Sanati S, Rezvani Z, Hou Z, Dai H. Ni–Ti Layered
862 Double Hydroxide@Graphitic Carbon Nitride Nanosheet: A Novel Nanocomposite
863 with High and Ultrafast Sonophotocatalytic Performance for Degradation of
864 Antibiotics. Inorganic Chemistry. 2019;58:1834-1849.
865 [56] Liu J, Li J, Bing X, Ng DHL, Cui X, Ji F, et al. ZnCr-LDH/N-doped graphitic
866 carbon-incorporated g-C_3N_4 2D/2D nanosheet heterojunction with enhanced charge
867 transfer for photocatalysis. Materials Research Bulletin. 2018;102:379-390.
868 [57] Han YY, Lu XL, Tang SF, Yin XP, Wei ZW, Lu TB. Metal-Free 2D/2D
869 Heterojunction of Graphitic Carbon Nitride/Graphdiyne for Improving the Hole
870 Mobility of Graphitic Carbon Nitride. Advanced Energy Materials. 2018;8:1702992.

871 [58] Su J, Li GD, Li XH, Chen JS. 2D/2D Heterojunctions for Catalysis. Advanced
872 Science. ;0:1801702.
873 [59] Shi L, Si W, Wang F, Qi W. Construction of 2D/2D layered g-C_3N_4/$Bi_{12}O_{17}Cl_2$
874 hybrid material with matched energy band structure and its improved photocatalytic
875 performance. RSC Advances. 2018;8:24500-24508.
876 [60] Shi J, Li S, Wang F, Gao L, Li Y, Zhang X, et al. 2D/2D g-C_3N_4/MgFe MMO
877 nanosheet heterojunctions with enhanced visible-light photocatalytic H_2 production.
878 Journal of Alloys and Compounds. 2018;769:611-619.
879 [61] Li Y, Zhang H, Liu P, Wang D, Li Y, Zhao H. Cross-Linked g-C_3N_4/rGO
880 Nanocomposites with Tunable Band Structure and Enhanced Visible Light
881 Photocatalytic Activity. Small. 2013;9:3336-3344.
882 [62] Ong WJ, Tan LL, Chai SP, Yong ST, Mohamed AR. Surface charge modification
883 via protonation of graphitic carbon nitride (g-C_3N_4) for electrostatic self-assembly
884 construction of 2D/2D reduced graphene oxide (rGO)/g-C_3N_4 nanostructures toward
885 enhanced photocatalytic reduction of carbon dioxide to methane. Nano Energy.
886 2015;13:757-770.
887 [63] Yuan L, Yang MQ, Xu YJ. Tuning the surface charge of graphene for
888 self-assembly synthesis of a $SnNb_2O_6$ nanosheet–graphene (2D–2D) nanocomposite
889 with enhanced visible light photoactivity. Nanoscale. 2014;6:6335-6345.
890 [64] Xu Q, Zhu B, Jiang C, Cheng B, Yu J. Constructing 2D/2D Fe_2O_3/g-C_3N_4 Direct
891 Z-Scheme Photocatalysts with Enhanced H_2 Generation Performance. Solar RRL.
892 2018;2:1800006.

893 [65] Fu J, Xu Q, Low J, Jiang C, Yu J. Ultrathin 2D/2D WO_3/g-C_3N_4 step-scheme
894 H_2-production photocatalyst. Applied Catalysis B: Environmental. 2019;243:556-565.
895 [66] Zhu B, Xia P, Ho W, Yu J. Isoelectric point and adsorption activity of porous
896 g-C_3N_4. Applied Surface Science. 2015;344:188-195.
897 [67] Yang YJ, Li W. Ultrasonic assisted coating of multiwalled carbon nanotubes with
898 NiFe-layered double hydroxide for improved electrocatalytic oxygen reduction.
899 Journal of Electroanalytical Chemistry. 2018;823:499-504.
900 [68] Mao N, Zhou CH, Tong DS, Yu WH, Cynthia Lin CX. Exfoliation of layered
901 double hydroxide solids into functional nanosheets. Applied Clay Science.
902 2017;144:60-78.
903 [69] Antonyraj CA, Koilraj P, Kannan S. Synthesis of delaminated LDH: A facile two
904 step approach. Chemical Communications. 2010;46:1902-1904.
905 [70] Zhang J, Chen Y, Wang X. Two-dimensional covalent carbon nitride nanosheets:
906 synthesis, functionalization, and applications. Energy & Environmental Science.
907 2015;8:3092-3108.
908 [71] Zhang X, Xie X, Wang H, Zhang J, Pan B, Xie Y. Enhanced Photoresponsive
909 Ultrathin Graphitic-Phase C3N4 Nanosheets for Bioimaging. Journal of the American
910 Chemical Society. 2013;135:18-21.
911 [72] Hong J, Zhang W, Wang Y, Zhou T, Xu R. Photocatalytic Reduction of Carbon
912 Dioxide over Self-Assembled Carbon Nitride and Layered Double Hydroxide: The
913 Role of Carbon Dioxide Enrichment. ChemCatChem. 2014;6:2315-2321.
914 [73] Nayak S, Mohapatra L, Parida K. Visible light-driven novel g-C_3N_4/NiFe-LDH

915 composite photocatalyst with enhanced photocatalytic activity towards water
916 oxidation and reduction reaction. Journal of Materials Chemistry A.
917 2015;3:18622-18635.
918 [74] Chu X, Wang J, Bai L, Dong Y, Sun W, Zhang W. Trimethylamine and ethanol
919 sensing properties of $NiGa_2O_4$ nano-materials prepared by co-precipitation method.
920 Sensors and Actuators B: Chemical. 2018;255:2058-2065.
921 [75] Moghadam AK, Mirzaee O, Shokrollahi H, Lavasani SANH. Magnetic and
922 morphological characterization of bulk $Bi_2Fe_4O_9$ derived by reverse chemical
923 co-precipitation: A comparative study of different sintering methods. Ceramics
924 International. 2019;45:8087-8094.
925 [76] Niu J, Qian H, Liu J, Liu H, Zhang P, Duan P. Process and mechanism of toluene
926 oxidation using $Cu_{1-y}Mn_2Ce_yO_x$/sepiolite prepared by the co-precipitation method.
927 Journal of Hazardous Materials. 2018;357:332-340.
928 [77] Theiss FL, Ayoko GA, Frost RL. Synthesis of layered double hydroxides
929 containing Mg^{2+}, Zn^{2+}, Ca^{2+} and Al^{3+} layer cations by co-precipitation methods—A
930 review. Applied Surface Science. 2016;383:200-213.
931 [78] Arif M, Yasin G, Shakeel M, Fang X, Gao R, Ji S, et al. Coupling of Bifunctional
932 CoMn-Layered Double Hydroxide@Graphitic C_3N_4 Nanohybrids towards Efficient
933 Photoelectrochemical Overall Water Splitting. Chemistry – An Asian Journal.
934 2018;13:1045-1052.
935 [79] Yuan X, Li W. Graphitic-C_3N_4 modified ZnAl-layered double hydroxides for
936 enhanced photocatalytic removal of organic dye. Applied Clay Science.

937 2017;138:107-113.

938 [80] Meng LY, Wang B, Ma MG, Lin KL. The progress of microwave-assisted
939 hydrothermal method in the synthesis of functional nanomaterials. Materials Today
940 Chemistry. 2016;1-2:63-83.

941 [81] Akbarzadeh R, Fung CSL, Rather RA, Lo IMC. One-pot hydrothermal synthesis
942 of g-C_3N_4/Ag/AgCl/$BiVO_4$ micro-flower composite for the visible light degradation
943 of ibuprofen. Chemical Engineering Journal. 2018;341:248-261.

944 [82] Xu Y, Liu T, Li Y, Liu Y, Ge F. Nanostructure Design and Catalytic Performance
945 of Mo/ZnAl-LDH in Cationic Orchid X-BL Removal. Materials. 2018;11:2390.

946 [83] Liu X, Liang J, Song X, Yang H, Li X, Dai H, et al. Enhanced water dissociation
947 performance of graphitic-C_3N_4 assembled with ZnCr-layered double hydroxide.
948 Chemical Engineering Journal. 2018;337:562-566.

949 [84] Yazdani D, Zinatizadeh AA, Jeshaghani M. Organic–inorganic Z-scheme
950 g-C_3N_4-NiTi-layered double hydroxide films for photocatalytic applications in a
951 fixed-bed reactor. Journal of Industrial and Engineering Chemistry. 2018;63:65-72.

952 [85] Demazeau G. Solvothermal reactions: an original route for the synthesis of novel
953 materials. Journal of Materials Science. 2008;43:2104-2114.

954 [86] Lai J, Niu W, Luque R, Xu G. Solvothermal synthesis of metal nanocrystals and
955 their applications. Nano Today. 2015;10:240-267.

956 [87] Dantelle G, Testemale D, Homeyer E, Cantarano A, Kodjikian S, Dujardin C, et
957 al. A new solvothermal method for the synthesis of size-controlled YAG:Ce
958 single-nanocrystals. RSC Advances. 2018;8:26857-26870.

959 [88] Zhang L, Li L, Sun X, Liu P, Yang D, Zhao X. ZnO-Layered Double
960 Hydroxide@Graphitic Carbon Nitride Composite for Consecutive Adsorption and
961 Photodegradation of Dyes under UV and Visible Lights. Materials. 2016;9:927.
962 [89] Ahmed N, Morikawa M, Izumi Y. Photocatalytic conversion of carbon dioxide
963 into methanol using optimized layered double hydroxide catalysts. Catalysis Today.
964 2012;185:263-269.
965 [90] Wang C, Zhang X, Xu Z, Sun X, Ma Y. Ethylene Glycol Intercalated
966 Cobalt/Nickel Layered Double Hydroxide Nanosheet Assemblies with Ultrahigh
967 Specific Capacitance: Structural Design and Green Synthesis for Advanced
968 Electrochemical Storage. ACS Applied Materials & Interfaces. 2015;7:19601-19610.
969 [91] Shakeel M, Arif M, Yasin G, Li B, Khan HD. Layered by layered
970 Ni-Mn-LDH/g-C_3N_4 nanohybrid for multi-purpose photo/electrocatalysis:
971 Morphology controlled strategy for effective charge carriers separation. Applied
972 Catalysis B: Environmental. 2019;242:485-498.
973 [92] Arif M, Yasin G, Shakeel M, Mushtaq MA, Ye W, Fang X, et al. Hierarchical
974 CoFe-layered double hydroxide and g-C_3N_4 heterostructures with enhanced
975 bifunctional photo/electrocatalytic activity towards overall water splitting. Materials
976 Chemistry Frontiers. 2019;3:520-531.
977 [93] Li C, Wei M, Evans DG, Duan X. Layered Double Hydroxide-based
978 Nanomaterials as Highly Efficient Catalysts and Adsorbents. Small.
979 2014;10:4469-4486.
980 [94] Yang Z, Wang F, Zhang C, Zeng G, Tan X, Yu Z, et al. Utilization of LDH-based

981 materials as potential adsorbents and photocatalysts for the decontamination of dyes
982 wastewater: a review. RSC Advances. 2016;6:79415-79436.
983 [95] Van Vaerenbergh B, De Vlieger K, Claeys K, Vanhoutte G, De Clercq J, Vermeir
984 P, et al. The effect of the hydrotalcite structure and nanoparticle size on the catalytic
985 performance of supported palladium nanoparticle catalysts in Suzuki cross-coupling.
986 Applied Catalysis A: General. 2018;550:236-244.
987 [96] Patnaik S, Sahoo DP, Mohapatra L, Martha S, Parida K. $ZnCr_2O_4$@ZnO/g-C_3N_4:
988 A Triple-Junction Nanostructured Material for Effective Hydrogen and Oxygen
989 Evolution under Visible Light. Energy Technology. 2017;5:1687-1701.
990 [97] Di G, Zhu Z, Huang Q, Zhang H, Zhu J, Qiu Y, et al. Targeted modulation of
991 g-C_3N_4 photocatalytic performance for pharmaceutical pollutants in water using
992 ZnFe-LDH derived mixed metal oxides: Structure-activity and mechanism. Science of
993 The Total Environment. 2019;650:1112-1121.
994 [98] Wang R, Pan K, Han D, Jiang J, Xiang C, Huang Z, et al. Solar-Driven H_2O_2
995 Generation From H_2O and O_2 Using Earth-Abundant Mixed-Metal Oxide@Carbon
996 Nitride Photocatalysts. ChemSusChem. 2016;9:2470-2479.
997 [99] Mureseanu M, Radu T, Andrei R-D, Darie M, Carja G. Green synthesis of
998 g-C_3N_4/CuONP/LDH composites and derived g-C_3N_4/MMO and their photocatalytic
999 performance for phenol reduction from aqueous solutions. Applied Clay Science.
1000 2017;141:1-12.
1001 [100] Lan M, Fan G, Yang L, Li F. Enhanced visible-light-induced photocatalytic
1002 performance of a novel ternary semiconductor coupling system based on hybrid

1003 Zn–In mixed metal oxide/g-C_3N_4 composites. RSC Advances. 2015;5:5725-5734.
1004 [101] Gao Z, Sasaki K, Qiu X. Structural Memory Effect of Mg–Al and Zn–Al
1005 layered Double Hydroxides in the Presence of Different Natural Humic Acids:
1006 Process and Mechanism. Langmuir. 2018;34:5386-5395.
1007 [102] Peng F, Wang D, Cao H, Liu X. Loading 5-Fluorouracil into calcined Mg/Al
1008 layered double hydroxide on AZ31 via memory effect. Materials Letters.
1009 2018;213:383-386.
1010 [103] Yuan X, Jing Q, Chen J, Li L. Photocatalytic Cr(VI) reduction by mixed metal
1011 oxide derived from ZnAl layered double hydroxide. Applied Clay Science.
1012 2017;143:168-174.
1013 [104] Li D, Lu M, Cai Y, Cao Y, Zhan Y, Jiang L. Synthesis of high surface area
1014 MgAl2O4 spinel as catalyst support via layered double hydroxides-containing
1015 precursor. Applied Clay Science. 2016;132-133:243-250.
1016 [105] Luo B, Song R, Jing D. ZnCr LDH nanosheets modified graphitic carbon nitride
1017 for enhanced photocatalytic hydrogen production. International Journal of Hydrogen
1018 Energy. 2017;42:23427-23436.
1019 [106] Salehi G, Abazari R, Mahjoub AR. Visible-Light-Induced
1020 Graphitic–C_3N_4@Nickel–Aluminum Layered Double Hydroxide Nanocomposites
1021 with Enhanced Photocatalytic Activity for Removal of Dyes in Water. Inorganic
1022 Chemistry. 2018;57:8681-8691.
1023 [107] Li K, Peng B, Peng T. Recent Advances in Heterogeneous Photocatalytic CO_2
1024 Conversion to Solar Fuels. ACS Catalysis. 2016;6:7485-7527.

1025 [108] Jo W-K, Tonda S. Novel CoAl-LDH/g-C_3N_4/RGO ternary heterojunction with
1026 notable 2D/2D/2D configuration for highly efficient visible-light-induced
1027 photocatalytic elimination of dye and antibiotic pollutants. Journal of Hazardous
1028 Materials. 2019;368:778-787.
1029 [109] Nayak S, Parida KM. Dynamics of Charge-Transfer Behavior in a
1030 Plasmon-Induced Quasi-Type-II p–n/n–n Dual Heterojunction in
1031 Ag@Ag_3PO_4/g-C_3N_4/NiFe LDH Nanocomposites for Photocatalytic Cr(VI)
1032 Reduction and Phenol Oxidation. ACS Omega. 2018;3:7324-7343.
1033 [110] Nayak S, Parida KM. Deciphering Z-scheme Charge Transfer Dynamics in
1034 Heterostructure NiFe-LDH/N-rGO/g-C_3N_4 Nanocomposite for Photocatalytic
1035 Pollutant Removal and Water Splitting Reactions. Scientific Reports. 2019;9:2458.
1036 [111] Tonda S, Jo W-K. Plasmonic Ag nanoparticles decorated NiAl-layered double
1037 hydroxide/graphitic carbon nitride nanocomposites for efficient visible-light-driven
1038 photocatalytic removal of aqueous organic pollutants. Catalysis Today.
1039 2018;315:213-222.
1040 [112] Low J, Jiang C, Cheng B, Wageh S, Al-Ghamdi AA, Yu J. A Review of Direct
1041 Z-Scheme Photocatalysts. Small Methods. 2017;1:1700080.
1042 [113] Zhao Y, Zhao Y, Waterhouse GIN, Zheng L, Cao X, Teng F, et al.
1043 Layered-Double-Hydroxide Nanosheets as Efficient Visible-Light-Driven
1044 Photocatalysts for Dinitrogen Fixation. Advanced Materials. 2017;29:1703828.
1045 [114] Li Y, Jin R, Xing Y, Li J, Song S, Liu X, et al. Macroscopic Foam-Like Holey
1046 Ultrathin g-C_3N_4 Nanosheets for Drastic Improvement of Visible-Light Photocatalytic

Activity. Advanced Energy Materials. 2016;6:1601273.

[115] Wang Q, Wang W, Zhong L, Liu D, Cao X, Cui F. Oxygen vacancy-rich 2D/2D BiOCl-g-C_3N_4 ultrathin heterostructure nanosheets for enhanced visible-light-driven photocatalytic activity in environmental remediation. Applied Catalysis B: Environmental. 2018;220:290-302.

Table 1
Constructing strategies and applications of some LDH/g-C_3N_4 binary photocatalysts.

Photocatalyst	Constructing strategy	Application	Reference
Mg-Al-LDH/g-C_3N_4	Electrostatic self-assembly	CO_2 reduction	[72]
Ni-Fe-LDH/g-C_3N_4	Electrostatic self-assembly	Water splitting	[73]
Zn-Cr-LDH/g-C_3N_4	Electrostatic self-assembly	Water splitting	[105]
Zn-Cr-LDH/modified g-C_3N_4	In-situ coprecipitation	Degradation of Congo red	[56]
Co-Mn-LDH/g-C_3N_4	In-situ coprecipitation	Water splitting	[78]
Zn-Al-LDH/g-C_3N_4	In-situ coprecipitation	Degradation of methylene blue	[79]
Ni-Al-LDH/g-C_3N_4	Hydrothermal method	CO_2 reduction	[53]
Co-Al-LDH/O-doped g-C_3N_4	Hydrothermal method	Degradation of methyl orange and bisphenol A	[54]
Ni-Ti-LDH/g-C_3N_4	Hydrothermal method	Degradation of amoxicillin	[55]
Zn-Cr-LDH/g-C_3N_4	Hydrothermal method	Water splitting	[83]
Ni-Ti-LDH/g-C_3N_4 film	Hydrothermal method	Degradation of methyl orange	[84]
Ni-Al-LDH/g-C_3N_4	Hydrothermal method	Degradation of rhodamine B and methyl orange	[106]
Zn-Al-LDH/g-C_3N_4	Solvothermal method	Degradation of methylene blue	[88]
Ni-Mn-LDH/g-C_3N_4	Solvothermal method	Degradation of rhodamine B	[91]
Co-Fe-LDH/g-C_3N_4	Solvothermal method	Water splitting	[92]

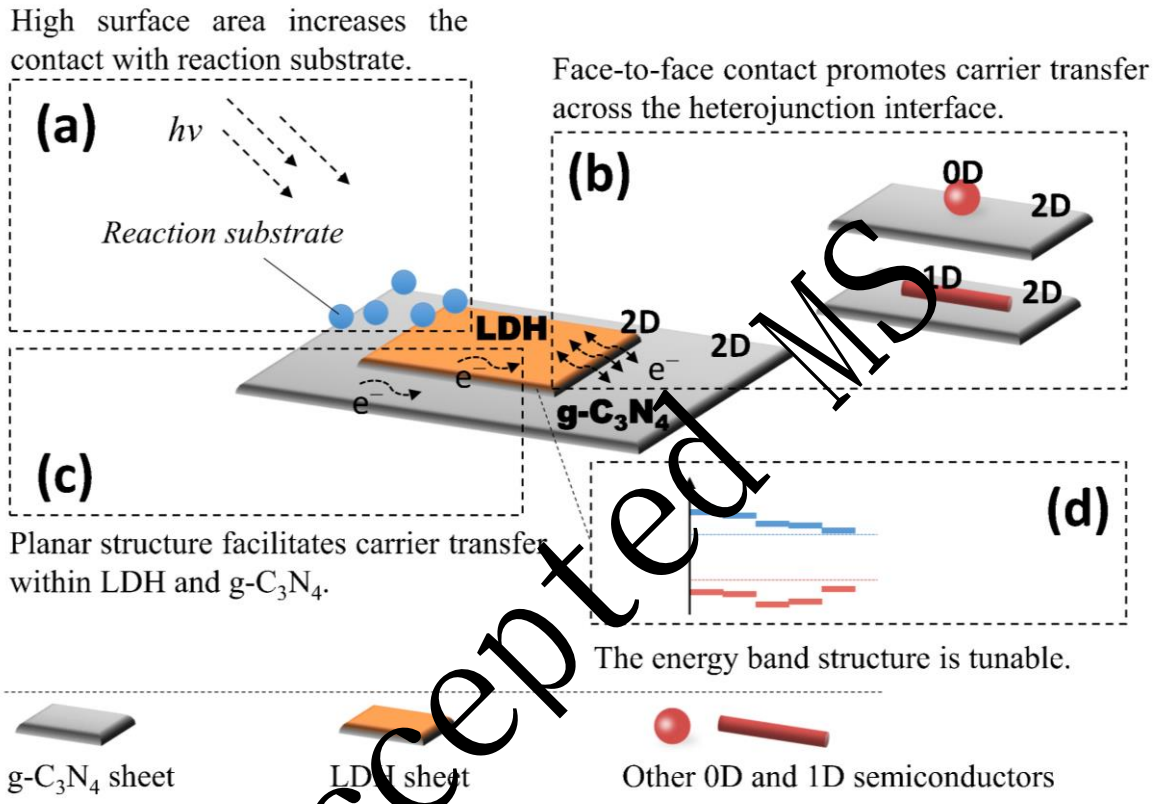

Fig. 1. Advantages of 2D/2D LDH/g-C_3N_4 heterostructure in photocatalytic applications.

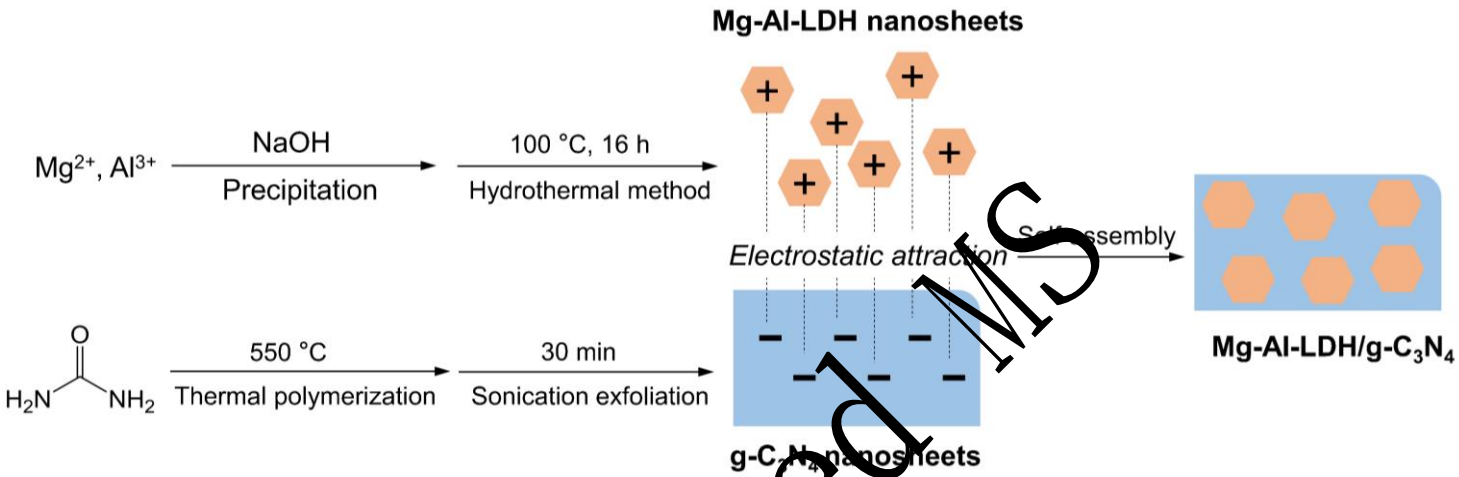

Fig. 2. Synthesis of Mg-Al-LDH/g-C_3N_4 photocatalyst by electrostatic self-assembly. This schematic diagram was drawn according to the method used by Hong et al. [72].

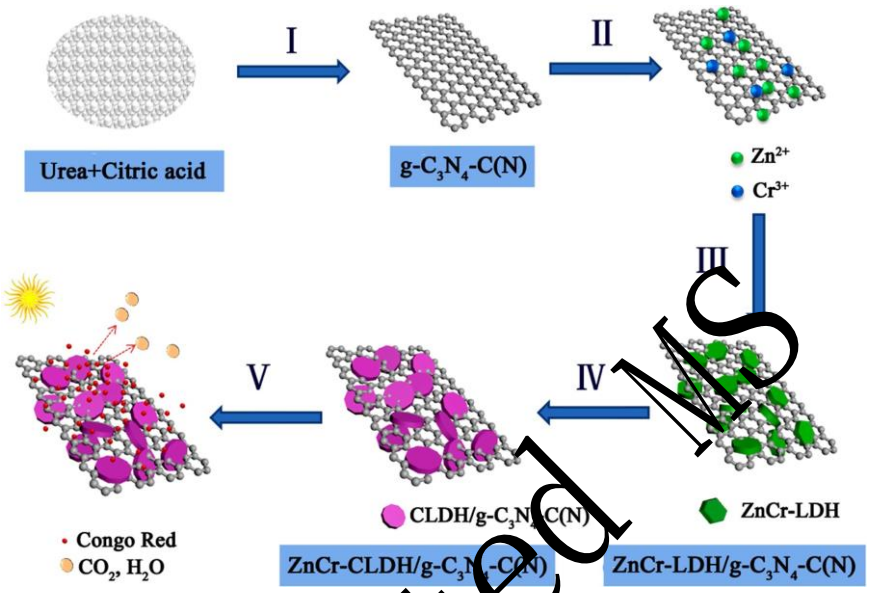

Fig. 3. Schematic illustration of the fabrication route of hybrid Zn-Cr-CLDH/g-C_3N_4-C(N) nanocomposites. (I) Thermal polymerization at 550 °C; (II) adding Zn^{2+} and Cr^{3+} under stirring; (III) in situ precipitation of Zn-Cr-LDH on g-C_3N_4-C(N); (IV) calcinations and formation of Zn-Cr-CLDH/g-C_3N_4-C(N); (V) adsorption and photocatalytic Congo red under visible light. Reproduced with permission from ref. [56]. Copyright 2018 Elsevier.

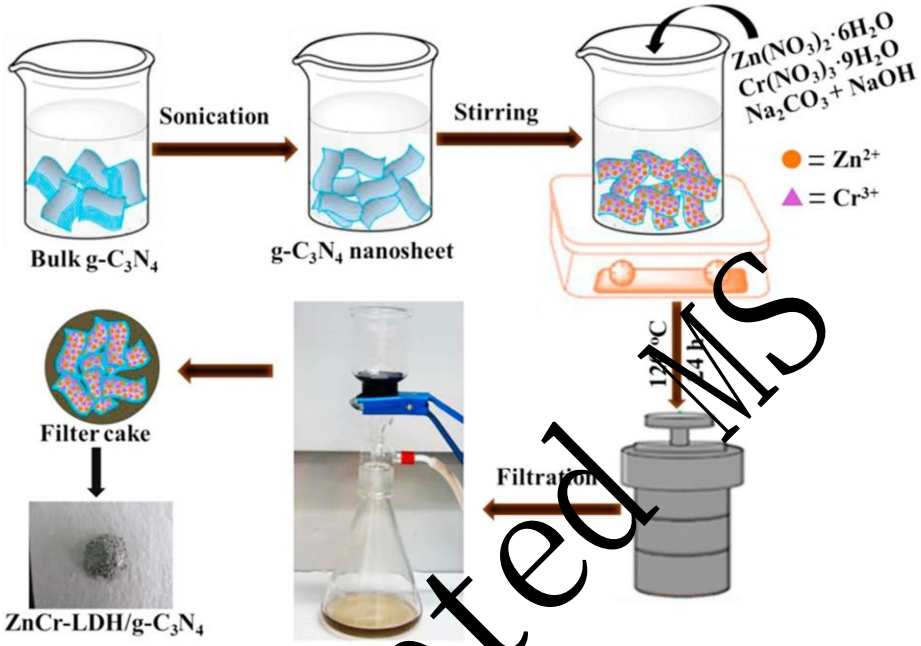

Fig. 4. Schematic representation of the synthesis process of the Zn-Cr-LDH/g-C_3N_4 composite. Reproduced with permission from ref. [83]. Copyright 2018 Elsevier.

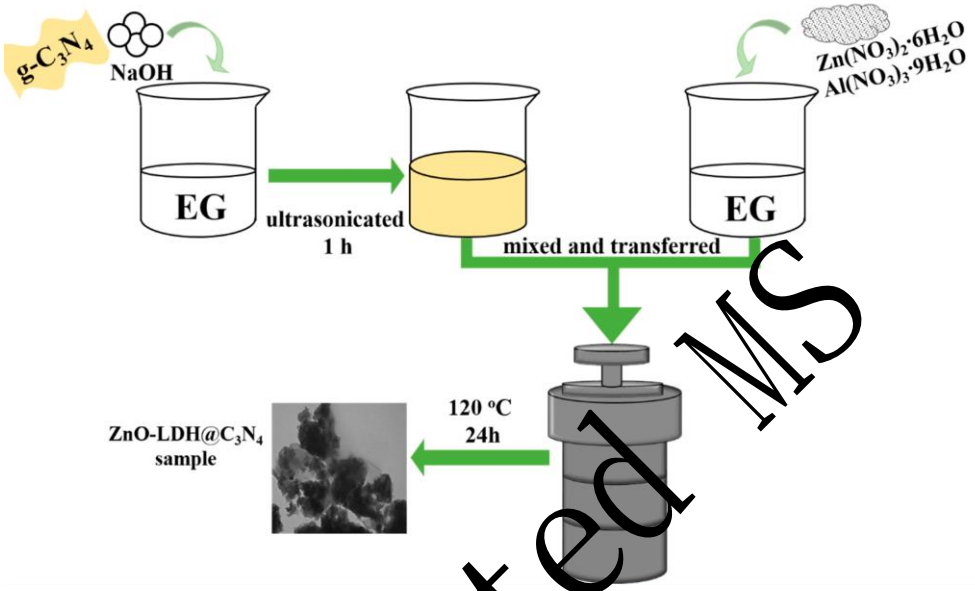

Fig. 5. Schematic representation of the synthesis process of the Zn-Al-LDH/g-C_3N_4 composite. Reproduced with permission from ref. [88]. Copyright 2016 The Authors.

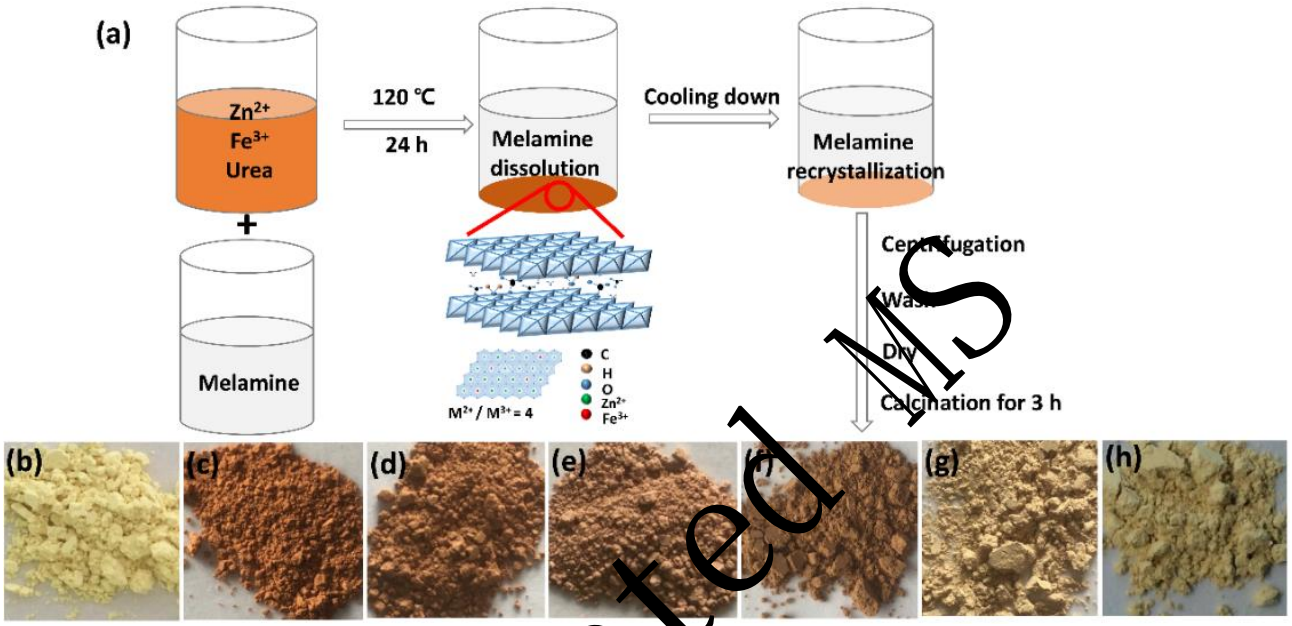

Fig. 6. (a) Schematic illustration of synthesizing the calcined Zn-Fe-LDH/g-C_3N_4 composites; photographs of the g-C_3N_4 (b), the calcined Zn-Fe-LDH (c), and the calcined Zn-Fe-LDH/g-C_3N_4 products with different weight percentages of g-C_3N_4 (d-h, from left to right: 0.5, 1.0, 5.0, 70, and 90 wt%). Reproduced with permission from ref. [97]. Copyright 2018 Elsevier.

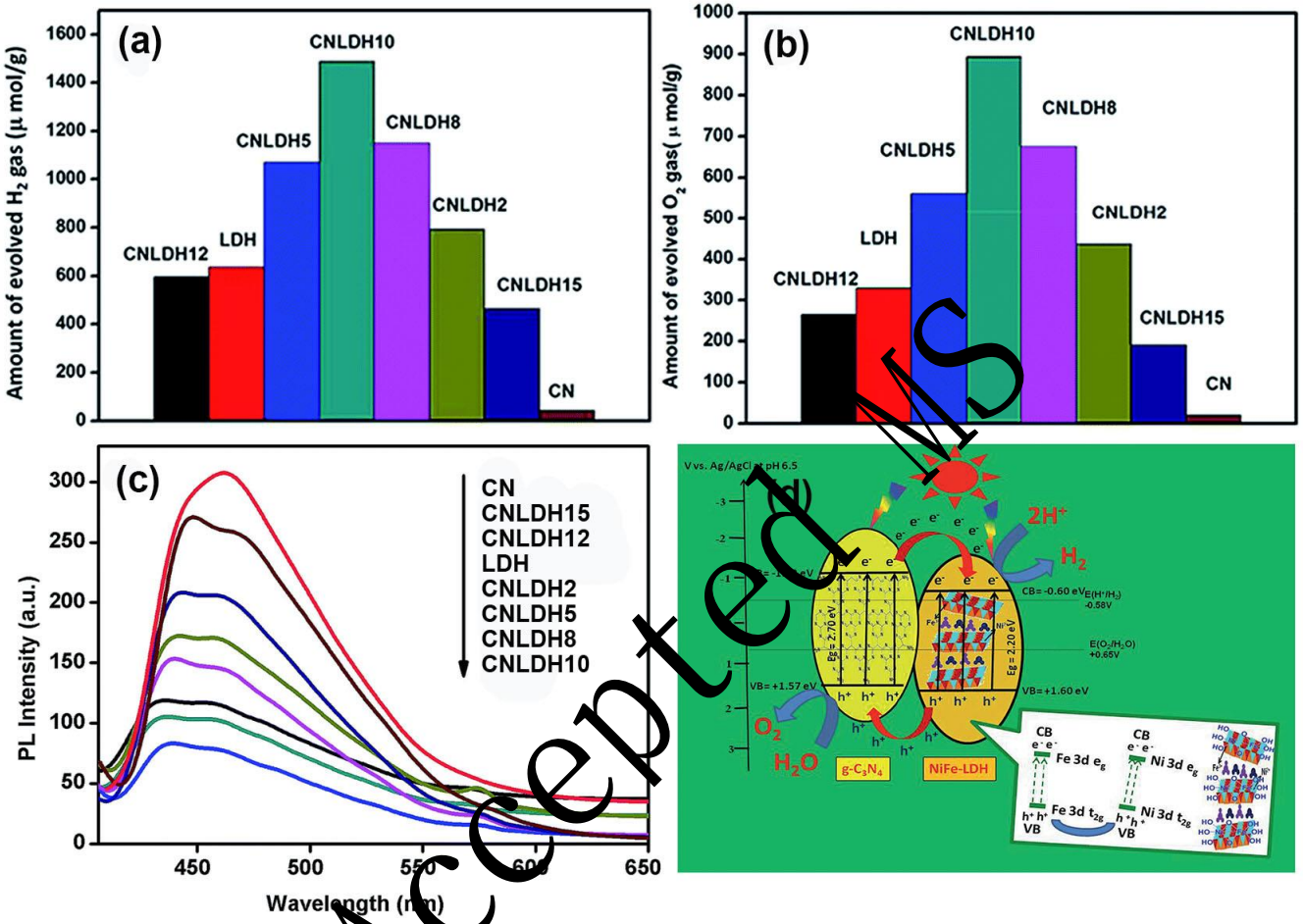

Fig. 7. (a) The amount of evolved hydrogen with Ni-Fe-LDH, g-C_3N_4 and different Ni-Fe-LDH/g-C_3N_4 composites in the photocatalytic water splitting; (b) the amount of evolved oxygen with Ni-Fe-LDH, g-C_3N_4 and different Ni-Fe-LDH/g-C_3N_4 composites in the photocatalytic water splitting; (c) photoluminescence spectra of Ni-Fe-LDH, g-C_3N_4 and different Ni-Fe-LDH/g-C_3N_4 composites; (d) proposed mechanism of the charge separation and transfer in Ni-Fe-LDH/g-C_3N_4 composites for the evolution of hydrogen and oxygen under visible light irradiation. CN: g-C_3N_4, LDH: Ni-Fe-LDH, CNLDHn: Ni-Fe-LDH/g-C_3N_4 containing n wt% g-C_3N_4. Reproduced with permission from ref. [73]. Copyright 2015 The Royal Society of Chemistry.

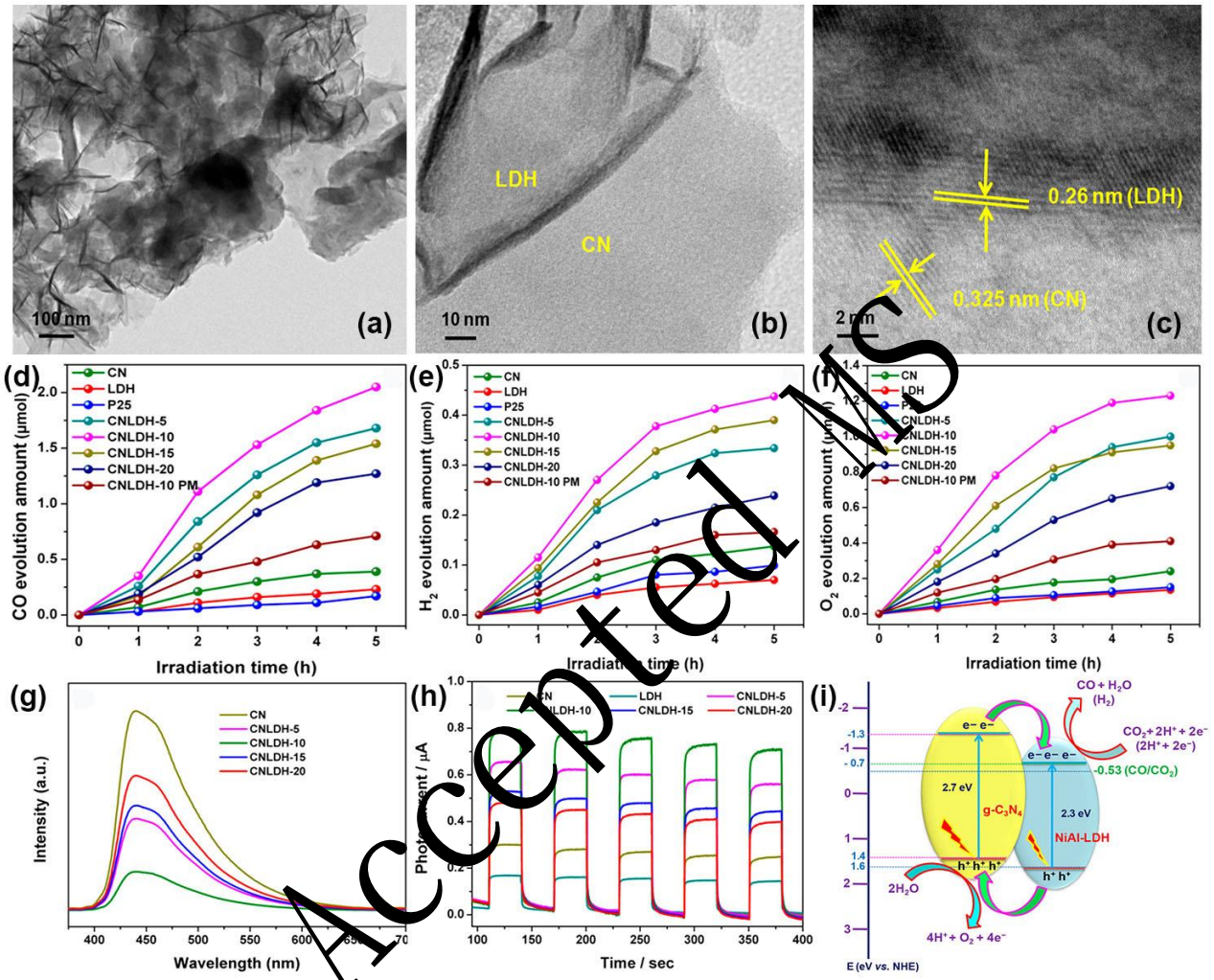

Fig. 8. (a and b) TEM images of CNLDH-10 composite; (c) high-resolution TEM image of CNLDH-10 composite; time-dependent evolution amount of (d) CO, (e) H_2, and (f) O_2 over all the synthesized photocatalysts under visible light irradiation; (g) PL spectra of g-C_3N_4, Ni-Al-LDH, and Ni-Al-LDH/g-C_3N_4; (h) transient photocurrent responses of g-C_3N_4, Ni-Al-LDH, and Ni-Al-LDH/g-C_3N_4; (i) proposed mechanism for CO_2 photoreduction by the Ni-Al-LDH/g-C_3N_4 photocatalyst. CN: g-C_3N_4, LDH: Ni-Al-LDH, CNLDH-n: Ni-Al-LDH/g-C_3N_4 containing n wt% Ni-Al-LDH, P25: commercial P25 reference catalyst, CNLDH-10 PM: physical mixture of Ni-Al-LDH (10 wt%) and g-C_3N_4. Reproduced with permission from ref. [53]. Copyright 2018 American Chemical Society.

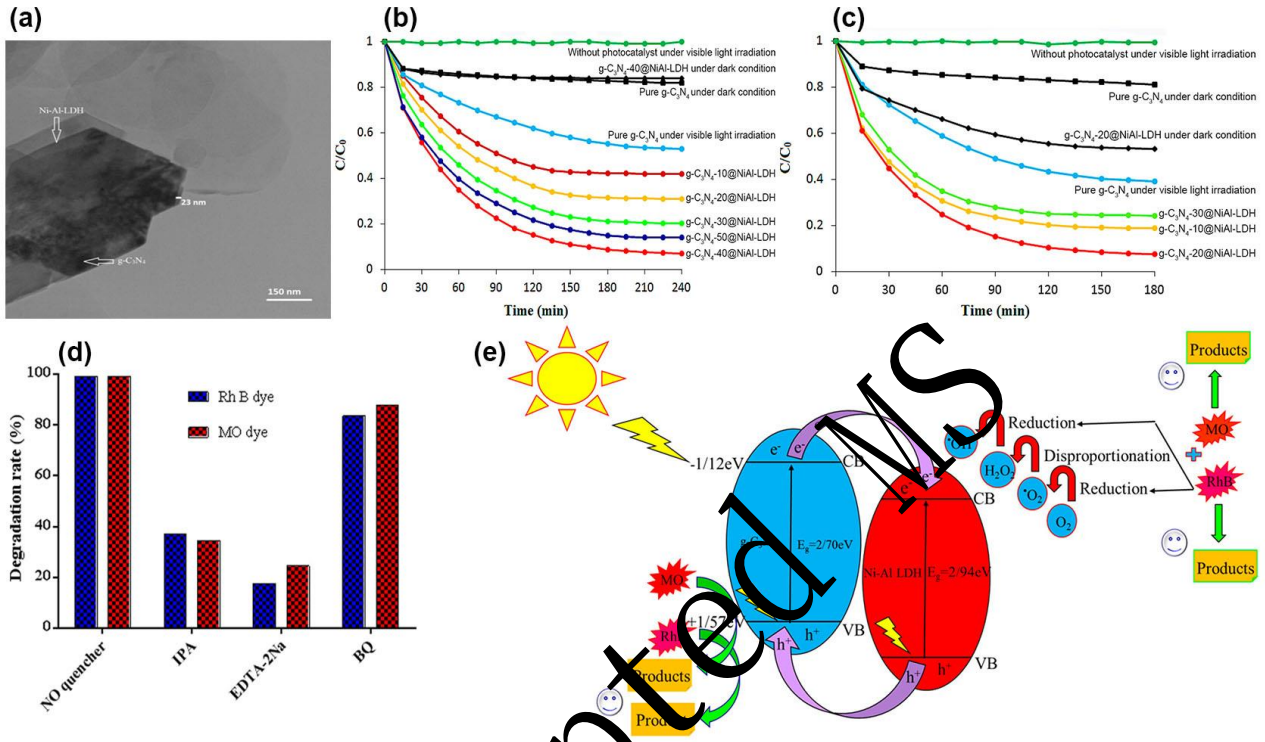

Fig. 9. (a) TEM image of the synthesized g-C_3N_4-40@NiAl-LDH composite; (b) photocatalytic activities for the degradation of rhodamine B under various conditions; (c) photocatalytic activities for the degradation of methyl orange under various conditions; (d) effects of various active scavengers on the degradation of rhodamine B by g-C_3N_4-40@NiAl-LDH and the degradation of methyl orange by g-C_3N_4-20@NiAl-LDH under visible light irradiation for 240 and 180 min, respectively; (e) possible mechanism for the photocatalytic degradation of rhodamine B and methyl orange by Ni-Al-LDH/g-C_3N_4 composite under visible light irradiation. g-C_3N_4-n@NiAl-LDH: Ni-Al-LDH/g-C_3N_4 composite containing n wt% g-C_3N_4, Rh B: rhodamine B, MO: methyl orange, IPA: isopropanol, BQ: p-benzoquinone. Reproduced with permission from ref. [106]. Copyright 2018 American Chemical Society.

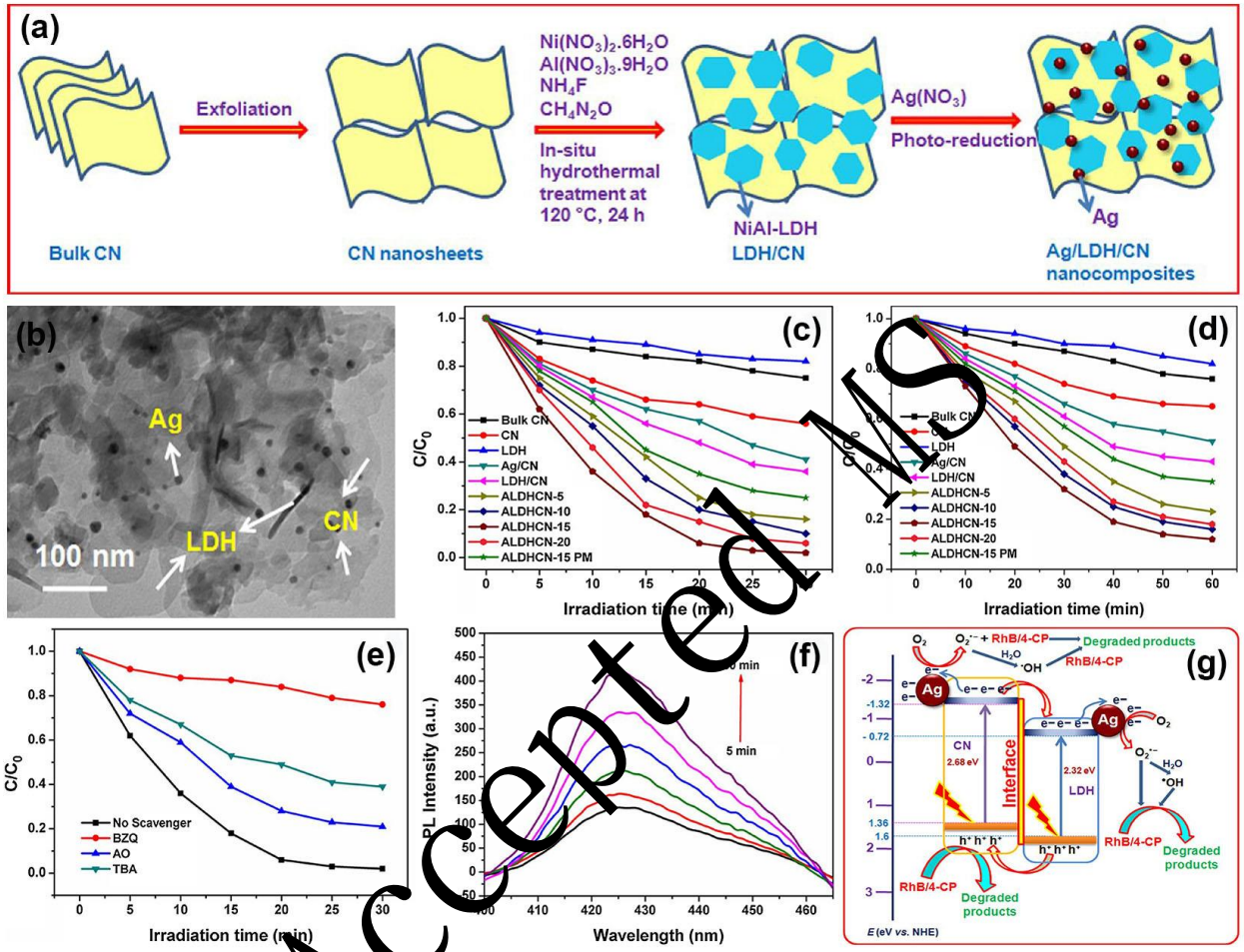

Fig. 10. (a) Schematic illustration of the synthesis of Ni-Al-LDH/g-C_3N_4/Ag face-to-face hybrid nanocomposites; (b) TEM images of the synthesized ALDHCN-15; (c) photocatalytic activities in the degradation of RhB over all the synthesized photocatalysts under visible light irradiation; (d) photocatalytic activities in the degradation of 4-CP over all the synthesized photocatalysts under visible light irradiation; (e) effects of different scavengers on the degradation of RhB with ALDHCN-15 under visible light irradiation; (f) $^{\cdot}OH$ trapping PL spectra of ALDHCN-15 in terephthalic acid solution under visible light irradiation; (g) schematic illustration of the charge separation and transfer in the Ni-Al-LDH/g-C_3N_4/Ag nanocomposite system under visible light irradiation. CN: g-C_3N_4, LDH: Ni-Al-LDH, ALDHCN-n: Ni-Al-LDH/g-C_3N_4/Ag containing n wt% Ni-Al-LDH, ALDHCN-15 PM: physical mixture of 15 wt% Ni-Al-LDH and CN (followed by 1 wt% Ag deposition), BZQ: benzoquinone, AO: ammonium oxalate, TBA: tert-butanol. Reproduced with permission from ref. [111]. Copyright 2017 Elsevier.

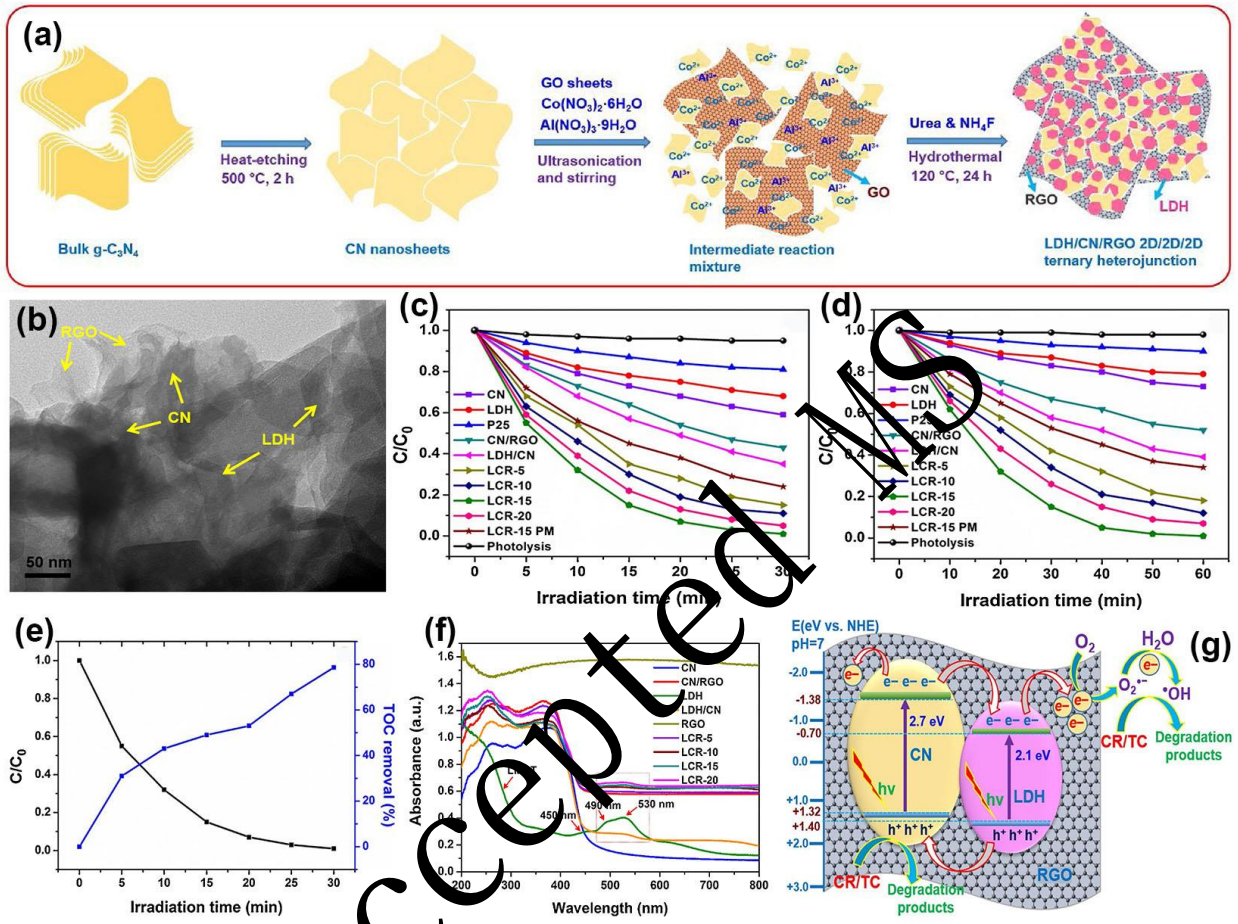

Fig. 11. (a) Schematic representation of the fabrication of Co-Al-LDH/g-C_3N_4/RGO 2D/2D/2D ternary heterojunction; (b) TEM image of LCR-15 photocatalyst; (c) the photocatalytic activities over all the fabricated catalysts in the degradation of CR; (d) the photocatalytic activities over all the fabricated catalysts in the degradation of TC; (e) comparison of the photocatalytic performance and TOC removal over the LCR-15 photocatalyst in the degradation of CR; (f) UV-vis DRS patterns of all the fabricated samples; (g) schematic diagram illustrating the photocatalytic mechanism for the degradation of CR and TC over the Co-Al-LDH/g-C_3N_4/RGO ternary heterojunction system. CN: g-C_3N_4, LDH: Co-Al-LDH, LCR-n: Co-Al-LDH/g-C_3N_4/RGO containing n wt% Co-Al-LDH, P25: commercial P25 reference catalyst, LCR-15 PM: physical mixture of 15 wt% Co-Al-LDH, 1 wt% RGO and g-C_3N_4. Reproduced with permission from ref. [108]. Copyright 2019 Elsevier.

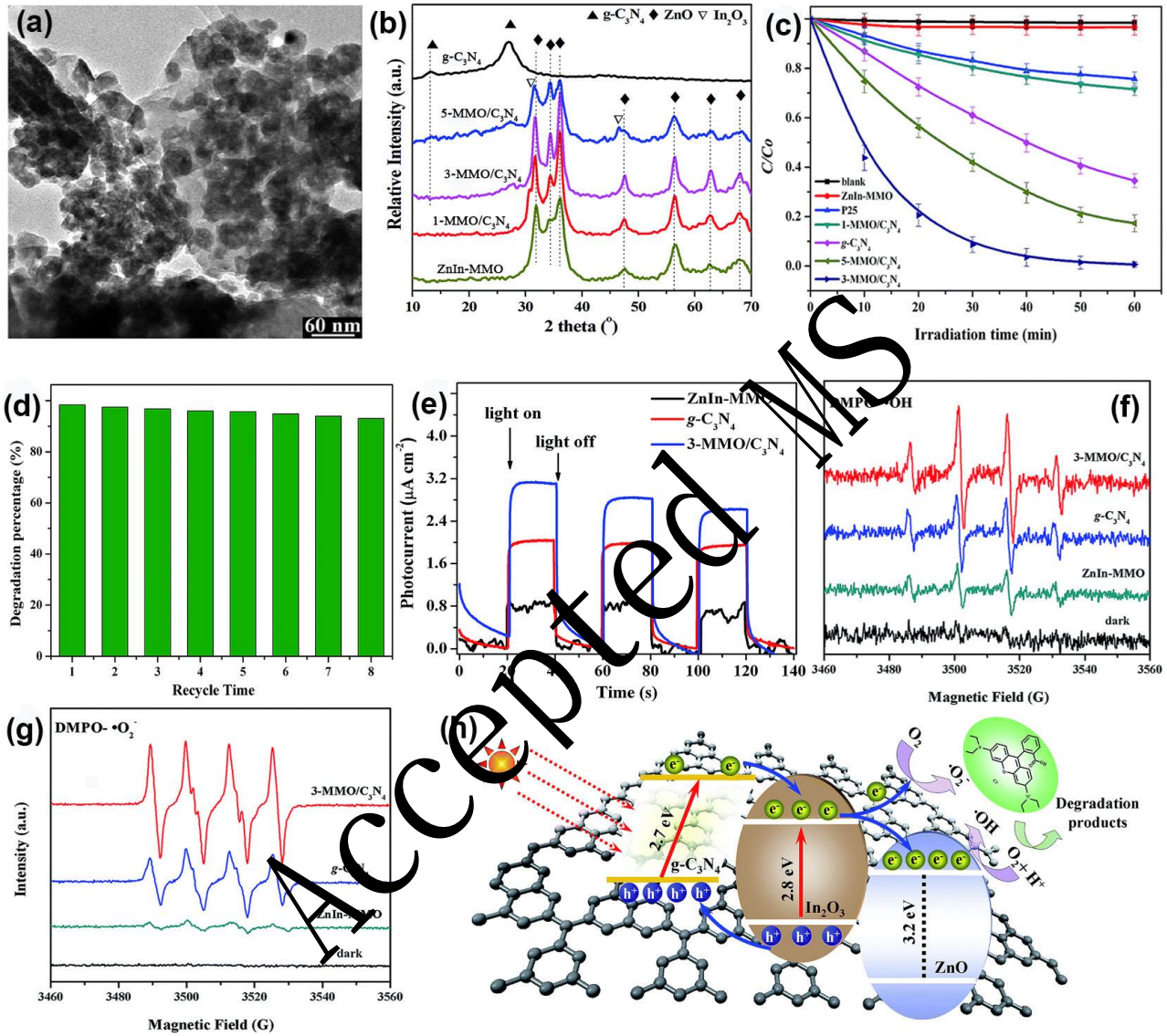

Fig. 12. (a) TEM image of 3-MMO/C_3N_4; (b) XRD patterns of all the prepared photocatalyst; (c) photocatalytic degradation of RhB over different photocatalysts under visible light irradiation; (d) cycling runs of 3-MMO/C_3N_4 in the photodegradation of RhB; (e) photocurrent profiles of ZnIn-MMO, g-C_3N_4 and 3-MMO/C_3N_4; (f) DMPO spin-trapping ESR spectra for DMPO- OH in aqueous solution; (g) DMPO spin-trapping ESR spectra for DMPO- O_2^- in dimethyl sulfoxide (DMSO); (h) proposed mechanism of charge separation and photocatalytic activity over ZnIn-MMO/g-C_3N_4 photocatalyst under visible light irradiation. Reproduced with permission from ref. [100]. Copyright 2015 The Royal Society of Chemistry.

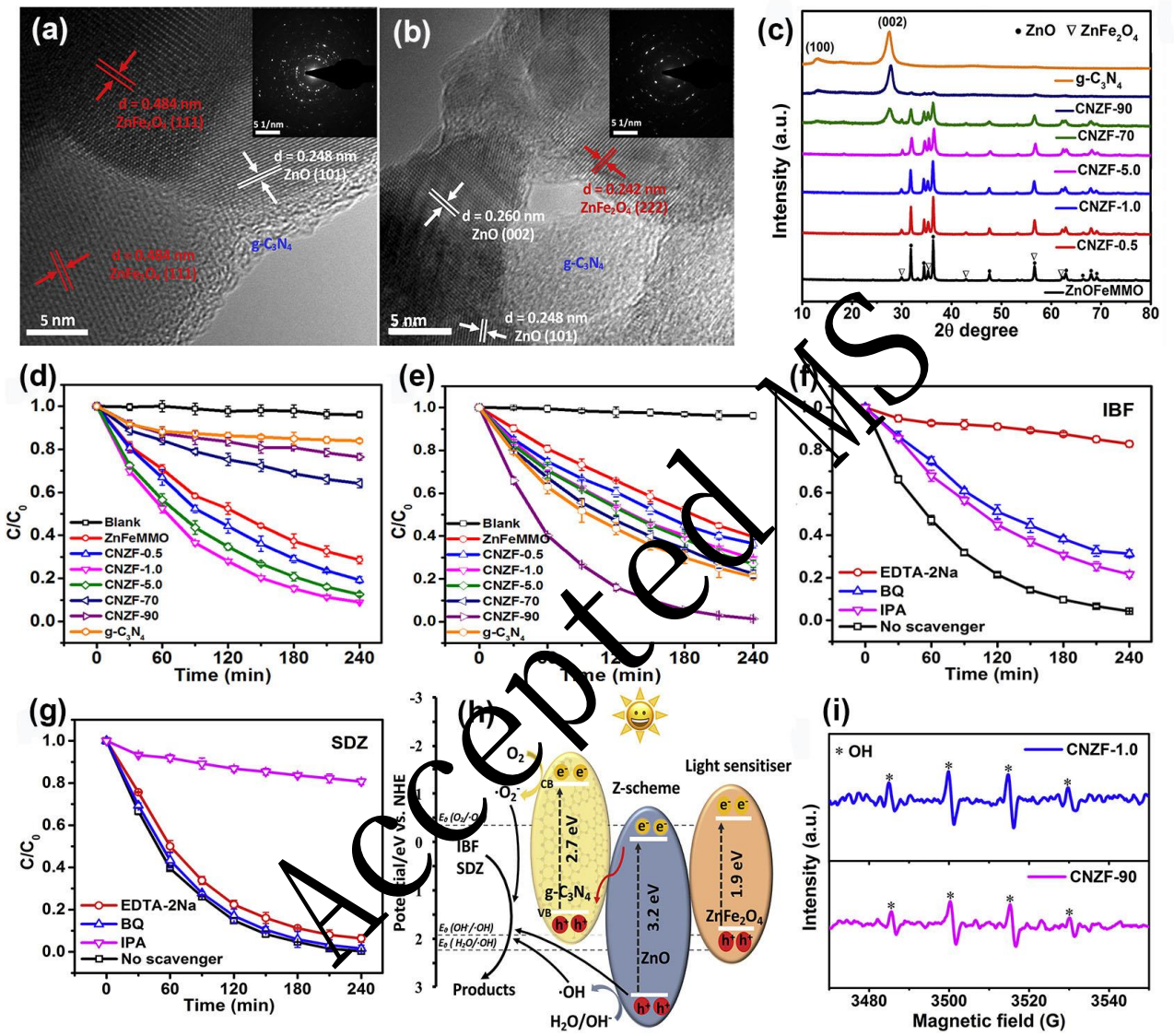

Fig. 13. (a-b) High-resolution TEM images and corresponding selected area electron diffraction (SAED) patterns of CNZF-1.0 and CNZF-90; (c) XRD patterns for all the prepared composites; (d) photodegradation of IBF over as-prepared photocatalysts under simulated solar irradiation; (e) photodegradation of SDZ over as-prepared photocatalysts under simulated solar irradiation; (f) IBF photodegradation over CNZF-1.0 in the presence of 1.0 mM various scavengers; (g) SDZ photodegradation over CNZF-90 in the presence of 1.0 mM various scavengers; (h) schematic illustration for the charge-transfer and photocatalytic mechanisms of calcined Zn-Fe-LDH/g-C_3N_4 composites. (i) EPR spectra of DMPO- OH over CNZF-1.0 and CNZF-90 upon irradiation for 5 min. ZnFeMMO: calcined Zn-Fe-LDH, CNZF-n: calcined Zn-Fe-LDH/g-C_3N_4 composites with n wt% of g-C_3N_4. Reproduced with permission from ref. [97]. Copyright 2018 Elsevier.